Highly resolved mapping of NO₂ vertical column densities from GeoTASO measurements over a megacity and industrial area during the KORUS-AQ campaign

Gyo-Hwang Choo[1], Kyunghwa Lee[1], Hyunkee Hong[1*], Ukkyo Jeong[2,3], Wonei Choi[4], Scott J. Janz[3]

[1]Environmental Satellite Center, National Institute of Environmental Research, Hwangyeong-ro 42, Seo-gu, Incheon, Republic of Korea, 22689

[2]Earth System Science Interdisciplinary Center, University of Maryland, College Park, Maryland, USA 20740

[3]NASA Goddard Space Flight Center, Greenbelt, Maryland, USA, 20771

[4]Division of Earth Environmental System Science, Major of Spatial Information Engineering, Pukyong National University, Busan 48513, South Korea

Correspondence to: Hyunkee Hong; Tel: +82 32 560 8437; Fax: +82 32 560 8460; E-mail address: wanju77@korea.kr

Abstract. The Korea-United States Air Quality (KORUS-AQ) campaign is a joint study between the United States National Aeronautics and Space Administration (NASA) and the South Korea National Institute of Environmental Research (NIER) to monitor megacity and transboundary air pollution around the Korean Peninsula using airborne and ground-based measurements. Here, tropospheric nitrogen dioxide (NO₂) slant column density (SCD) measurements were retrieved from Geostationary Trace and Aerosol Sensor Optimization (GeoTASO) L1B data during the KORUS-AQ campaign (May 1 to June 10, 2016). The retrieved SCDs were converted to tropospheric vertical column densities using the air mass factor (AMF) obtained from a radiative transfer calculation with trace gas profiles and aerosol property inputs simulated with the Community Multiscale Air Quality (CMAQ) model and surface reflectance data obtained from the Moderate Resolution Imaging Spectroradiometer (MODIS). For the first time, we examine highly resolved (250 m × 250 m resolution) tropospheric NO₂ over the Seoul and Busan metropolitan regions, and the industrial regions of Anmyeon. We reveal that the maximum NO₂ VCDs were 4.94×10^{16} and 1.46×10^{17} molecules cm⁻² at 9 AM and 3 PM over Seoul, respectively, 6.86×10^{16} and 4.89×10^{16} molecules cm⁻² in the morning and afternoon over Busan, respectively, and 1.64×10^{16} molecules cm⁻² over Anmyeon. The VCDs retrieved from the GeoTASO airborne instrument were well correlated with those obtained from the Ozone Monitoring Instrument (OMI) (r = 0.70), NASA's Pandora Spectrometer System (r = 0.79), and NO₂ mixing ratios obtained from in situ measurements (r = 0.45 in the morning, r = 0.81 in the afternoon over the Seoul, and r > 0.78 over Busan). Based on our results, GeoTASO is useful for identifying hotspots of NO₂ and its spatial distribution in highly populated cities and industrial areas.

1 Introduction

Nitrogen dioxide (NO$_2$) is one of the most important atmospheric trace gases and plays a key role in aerosol production and tropospheric ozone photochemistry (Boersma et al., 2004; Richter et al., 2005). Furthermore, high NO$_2$ concentrations in the atmosphere have adverse effects on human health, such as respiratory infections, domestic heating, and associated symptoms (Brauer et al., 2002; Latza et al., 2009).

The major sources of NO$_2$ in the atmosphere are from fossil fuel combustion from vehicles and thermal power plants, lightning, flash production, and biogenic soil processes. In addition, it has been found that NO$_2$ concentrations are highly correlated with population size (Lamsal et al., 2013). The implementation of emission control technology and environmental regulation has led to a decrease in surface NO$_2$ concentrations in Western Europe, the United States, and Japan in the last few decades (Richter et al., 2005). The NO$_2$ concentration over major metropolitan cities in South Korea and China are over 3 times larger than over similarly sized cities in Europe and United States, despite NO$_2$ concentration decreasing in China and South Korea (de Foy et al., 2016, Choo et al., 2020).

To date, several low-orbit space borne sensors, such as the Global Ozone Monitoring Experiment (GOME) (Burrows et al., 1999), the Scanning Imaging Spectrometer for Atmospheric Cartography (SCIAMACHY) (Burrows et al., 1995), the Ozone Monitoring Instrument (OMI) (Levelt et al., 2006), the GOME-2 (Callies et al., 2000), and the Tropospheric Monitoring Instrument (TROPOMI) (Veefkind et al., 2012), have monitored atmospheric ozone and its precursors including NO$_2$ and formaldehyde (HCHO) as a proxy for volatile organic compounds (VOCs). Furthermore, the Geostationary Environment Monitoring Spectrometer (GEMS) (Choi et al., 2018; Kim et al., 2020), which was launched on February 18, 2020, will form a constellation of geostationary satellites including the upcoming Tropospheric Emission: Monitoring of Pollution (TEMPO) (Zoogman et al., 2017) and Sentinel-4 platforms, to continuously observe the air quality of the Northern Hemisphere during the daytime.

NO$_2$ retrievals from space borne hyperspectral measurements are typically conducted using the differential optical absorption spectroscopy (DOAS) method (Platt and Stutz, 2008) to first retrieve the view-dependent slant column density (SCD), and then radiative transfer models are used to determine the vertical column density (VCD) using an air mass factor (AMF) correction. Previous and ongoing space borne instruments use various radiative transfer codes and model input assumptions to calculate NO$_2$ AMF values at fairly coarse spatial resolution. Because the AMF weighting has a large impact on NO$_2$ retrievals using the DOAS method, it is important to use model input assumptions that most accurately match the viewing and atmospheric conditions. Several studies have demonstrated the sensitivity of AMF calculations to inaccurate model input parameters (e.g., *a priori* NO$_2$ vertical profile and aerosol properties) and *a priori* data (cloud information and surface reflectance) (Leitão et al., 2010; Hong et al., 2017; Lorente et al., 2017; Boersma et al., 2018). NO$_2$ retrievals have also been consistently conducted based on surface remote sensing measurements including the Multi-Axis DOAS (MAX-DOAS), Système D'Analyse par Observations Zènithales (SAOZ) spectrometer (Pastel et al., 2014), and Pandora (Herman et al., 2009)

61 systems. These ground-based measurements can be used as validation references for both airborne and space borne

62 measurements.

63 Furthermore, NO_2 retrievals from airborne remote sensing instruments, such as the Geostationary Coast and Air Pollution

64 Event (GEO-CAPE) Airborne Simulator (GCAS) (Kowalewski and Janz, 2014), the Heidelberg Airborne Imaging DOAS

65 Instrument (HAIDI) (General et al., 2014), the Geostationary Trace gas and Aerosol Sensor Optimization (GeoTASO) (Leitch

66 et al., 2014), the Airborne Prism Experiment (APEX; Popp et al., 2012), the Airborne Imaging DOAS instrument for

67 Measurements of Atmospheric Pollution (AirMAP; Meier et al., 2017; Schönhardt et al., 2015), the Small Whiskbroom Imager

68 for atmospheric compositioN monitorinG (SWING; Merlaud et al. 2018), and the Spectrolite Breadboard Instrument (SBI;

69 Vlemmix et al., 2017; Tack et al., 2019) have also been performed to identify local emission sources and obtain highly resolved

70 horizontal NO_2 distributions.

71 Observations using airborne measurements have an advantage as they enable the observation of horizontal distributions of

72 trace gases at resolutions higher than space-based satellites and provide data over a wider area than ground-based observations.

73 For example, Nowlan et al. (2018) retrieved tropospheric NO_2 VCDs over Houston, Texas, during the Deriving Information

74 on Surface Conditions from Column and Vertically Resolved Observations Relevant to Air Quality (DISCOVER-AQ)

75 campaign and identified a high correlation with data retrieved from Pandora. Popp et al. (2012) also presented the morning

76 and afternoon NO_2 spatial distribution in Zurich, Switzerland, using APEX. Tack et al. (2017) have conducted high-resolution

77 mapping of NO_2 over three Belgium cities (Antwerp, Brussels, and Liège) using APEX and Judd et al. (2020) and Tack et al.

78 (2021) compared NO_2 VCDs retrieved from GCAS/GeoTASO and APEX with those obtained from TROPOMI over New

79 York City and Antwerp and Brussels, respectively. Merlaud et al. (2013) observed NO_2 VCDs in Turceni over Romania using

80 SWING mounted on an unmanned aerial vehicle (UAV) during the Airborne Romanian Measurements of Aerosols and Trace

81 gases (AROMAT) campaign. These existing NO_2 retrievals, using airborne measurements, have been useful for constraining

82 regional air quality models due to the highly resolved source identification and the ability to tie these results to the ground-

83 based observations.

84 This work focuses on airborne NO_2 retrievals from GeoTASO. This instrument was developed by Ball Aerospace to reduce

85 mission risk for the UV-VIS air quality measurements from geostationary orbit for the GEMS and TEMPO missions (Leitch

86 et al., 2014). The retrieval of NO_2, SO_2, and HCHO observed from GeoTASO L1B data using DOAS and principal component

87 analysis (PCA) (Wold et al., 1987) was conducted through the DISCOVER-AQ and KORea-United States Air Quality

88 (KORUS-AQ) campaigns (Nowlan et al., 2016; Judd et al., 2018; Choi et al., 2020; Chong et al., 2020). The KORUS-AQ

89 campaign is a joint study between the National Institute of Environmental Research (NIER) and National Aeronautics and

90 Space Administration (NASA) to monitor megacity air pollution and transboundary pollution, and to prepare for geostationary

91 satellite (i.e., GEMS, TEMPO, and Sentinel-4) air quality observability (of trace gases and aerosols), organized from May to

92 June 2016.

93 Although surface NO_2 concentrations in South Korea are high due to high population density, high traffic volumes, and many

94 industrial complexes and thermal power plants, and whereas NO_2 retrieval studies using airborne and ground measurements

over North America, Europe, China, and Japan have been conducted, data for South Korea remain limited. The specific aims of this study are as follows:

    (1) To retrieve tropospheric NO_2 vertical column data using GeoTASO measurements over polluted regions of the Seoul and Busan metropolitan areas and the Anmyeon industrial regions of the Korean Peninsula.

    (2) To estimate NO_2 VCD uncertainties using error propagation accounting for spectral fitting errors and AMF uncertainties associated with input data errors, including aerosol optical depth (AOD), single scattering albedo (SSA), aerosol loading height (ALH), and surface reflectance.

    (3) To compare NO_2 VCDs retrieved from GeoTASO and those obtained from OMI and ground-based Pandora instruments, as well as surface in situ measurements.

2 KORUS-AQ campaign area, measurements, and model simulation

2.1 Campaign area
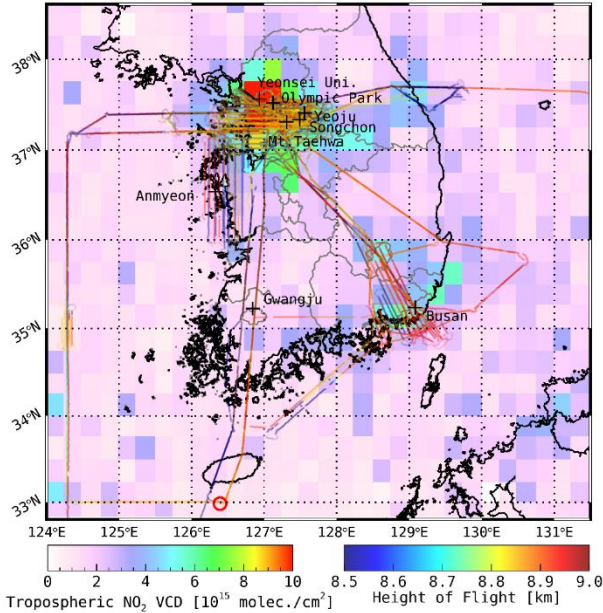
Figure 1. Flight paths of the NASA LaRC B200 aircraft carrying GeoTASO and the average tropospheric NO_2 VCDs obtained from OMI gridded to a 0.25°×0.25° horizontal grid during the KORUS-AQ campaign period. The line colour represents flight height. In this period, the GeoTASO observations focused on megacities (Seoul and Busan) and industrial complex area (Anmyeon) with high tropospheric NO_2 concentrations. The reference spectrum for spectral fitting is obtained from the radiation data under the Jeju Island (marked with red circle).

The Korean Peninsula, located on the Asia-Pacific coast, has a complex atmospheric environment by local emissions and long-range transport under appropriate weather conditions (Jeong et al., 2017; NIER and NASA, 2020; Choo et al., 2021). In

4

115 particular, Seoul, the capital of South Korea, and the metropolitan area are densely populated, and power plants and industrial

116 activities on the northwest coast are carried out, which emits relatively large amounts of pollutants. The KORUS-AQ campaign

117 conducted three-dimensional observations, including ground-based remote, aircraft, satellite observation, and air quality

118 modelling, to understand the complex air quality and interpret the observations of GEMS launched in 2020. The KORUS-AQ

119 campaign period was from May 2 to June 10, 2016. During the KORUS-AQ campaign, measurements of air pollutants were

120 carried out by using the GeoTASO on board the NASA Langley Research Center B200 aircraft to monitor air quality and long-

121 range transport of pollutants over the Korean Peninsula (NIER and NASA, 2020). The GeoTASO observations conducted a

122 total of 30 times over 23 days out of 40 days. Most observations were made once or twice a day. Each flight were planned and

123 conducted on a day when weather conditions were fine and flight hours were approximately 2-4 hours. Flight information on

124 the date of aircraft observation can be found in detail at http://www-air.larc.nasa.gov/missions/korus-aq/docs/KORUS-

125 AQ_Flight_Summaries_ID122.pdf. Figure 1 shows the flight routes of B200 and the tropospheric NO_2 VCDs obtained from

126 the OMI during the campaign period. The observations were concentrated in the metropolitan areas of Seoul and Busan and

127 the industrial areas of Anmyeon, with a flight altitude of 8,000–9,000 m.

128 As shown in Fig. 1, GeoTASO observations were conducted focusing on highly NO_2-polluted regions in the Seoul and Busan

129 metropolitan areas and the Anmyeon region during the KORUS-AQ campaign. The Seoul metropolitan area (Seoul Special

130 City, Gyeonggi Province, and Incheon City) is one of the most densely populated areas worldwide, with a population of

131 approximately 20 million in 2016. Busan is the second-largest city in South Korea, with a population of approximately 3.4

132 million in 2016. Anmyeon is located southwest of Seoul with petrochemical complexes, steel mill works, and thermal power

133 stations in this area. The background colour in Fig. 1 represents the average NO_2 VCD obtained from the OMI during the

134 KORUS-AQ campaign period, showing over 1×10^{16} molecules cm^{-2} over the Seoul metropolitan area. The OMI data obtained

135 by the Level 2.0 OMNO2 version 3.0 and downloaded from the NASA's Earthdata search

136 (http://search.earthdata.nasa.gov/search/). We calculated the arithmetic means of the tropospheric NO_2 VCDs, similar to Choo

137 et al. (2020), to obtain the grid data (0.25° × 0.25°) during KORUS-AQ period. The average tropospheric NO_2 VCD data were

138 excluded from 30 May 2016 to 9 Jun 2016, when the OMI data did not exist during the campaign period.

2.2 Pandora

140 NO_2 VCDs retrieved from the GeoTASO were validated using those from NASA's Pandora Spectrometer system. The Pandora

141 spectrometer is a hyper-spectrometer that can provide direct sun measurements of UV/Vis spectra (280–525 nm with a full

142 width at half maximum (FWHM) of 0.6 nm) for observing atmospheric trace gases. During the KORUS-AQ, eight Pandora

143 instruments monitored NO_2 and ozone (O_3) VCD as depicted by plus symbols in Fig. 1. The retrieved data are available on the

144 KORUS-AQ pages of NASA's Goddard Space Flight Center website

145 (https://avdc.gsfc.nasa.gov/pub/DSCOVR/Pandora/DATA/KORUS-AQ/). We compared NO_2 VCDs obtained from five

146 Pandora measurement (Busan university: 35.24 °N, 129.08 °E; Olympic park: 37.52 °N, 127.13 °E: Songchon: 37.41 °N,

147 127.56 °E; Yeoju: 37.34 °N, 127.49 °E; Yonsei University: 37.56 °N, 126.93 °E) within 0.05 degree and 30 min with those

148 from GeoTASO. Because NO_2 has a short atmospheric lifetime, especially during the summer (Shah et al., 2020), its spatial

149 and temporal distributions vary notably. A detailed description of Pandora's operation during the KORUS-AQ campaign has

150 been previously reported (Herman et al., 2018; Spinei et al., 2018).

151 **2.3 Ground-based in situ NO_2 measurement**

152 Although the basic physical quantity of VCD and surface mixing ratio from in-situ measurements are different, comparison of

153 their spatiotemporal variations provides useful information for deriving surface air quality from airborne instruments (e.g.,

154 Jeong and Hong, 2021a; 2021b *and references therein*). In this study, we compare the NO_2 VCDs (molecules cm^{-2}) retrieved

155 from GeoTASO to surface mixing ratios measured by ground-based in-situ monitoring network over South Korea (i.e., Air-

156 Korea, a national real-time air quality network; https://www.airkorea.or.kr/). The instruments utilize the chemiluminescence

157 method (Kley and McFarland, 1980), and approximately 400 air quality monitoring sites in Korea are registered in the system,

158 providing hourly surface NO_2 concentrations. We compared NO_2 VCDs retrieved from GeoTASO within 0.5 km and 30 min

159 with NO_2 concentrations obtained from Air-Korea.

160 **2.4 GeoTASO measurements**

161 NO_2 VCDs were retrieved from the L1B radiance dataset (version: V02y) obtained using GeoTASO during the KORUS-AQ

162 campaign. The NASA Goddard Space Flight Center conducted the L1B radiance calibration, which included offset and smear

163 correction, gain matching, amplifier cross-talk correction, dark rate correction, integration normalisation, sensitivity derivation,

164 wavelength registration, geo-registration, non-linearity correction, and ground pixel geolocation (Kowalewski et al., 2017;

165 Chong et al., 2020). The detailed specifications of GeoTASO are listed in Table 1.

166

167 **Table 1. Summary for GeoTASO instrument and optical specification.**

L1B version	V02y
Cross-track field of view	45°
Wavelength	UV: 290–400 nm
	VIS: 415–695 nm
Spectral resolution (full width at half maximum, FWHM)	UV: ~0.39 nm
	VIS: ~0.88 nm
CCD	1,056 (wavelength) × 1,033 (cross-track)
Spatial resolution before binning	~35 m (along-track) × 7 m (cross-track)

| Spatial resolution after binning | ~250 m (along-track) × 250 m (cross-track) |

168

169

170

171
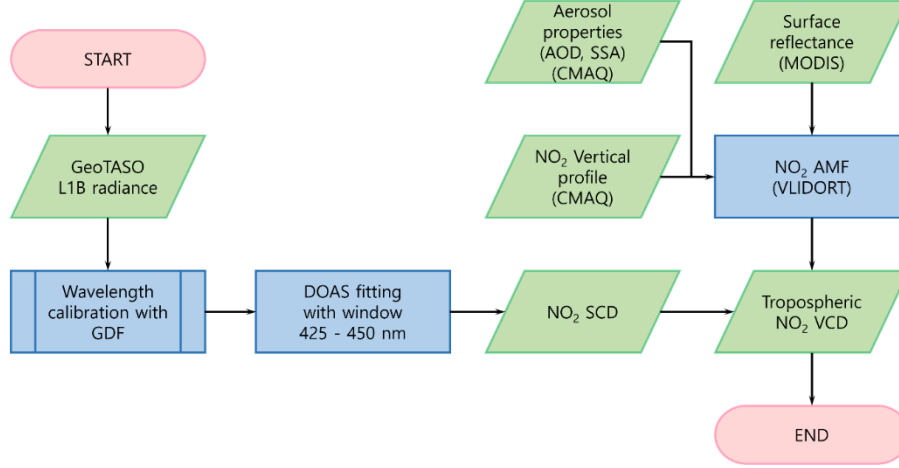
Figure 2. Flowchart of the algorithm for retrieving tropospheric NO₂ data from GeoTASO.

173

2.4.1 NO₂ slant column density retrieval

Figure 2 shows the flowchart for retrieving the tropospheric NO_2 VCD from the GeoTASO. We first retrieved NO_2 SCDs using the DOAS method (Platt, 1994). Nonlinear least square minimisation was used to retrieve the NO_2 SCDs which minimize the difference between the measured optical depth and the modelled value in QDOAS software (Eq. (1); Danckaert et al., 2012).

$$\frac{\ln I(\lambda)}{\ln I_0(\lambda)} = -\left(\sum_{j=1}^{m} \rho_j \times \sigma'_j(\lambda) + B(\lambda) + R(\lambda) + A(\lambda) + N(\lambda)\right) \tag{1}$$

Where $I(\lambda)$ is the measured earthshine radiance at wavelength λ; I_0 is the reference radiance from the sea surface south of Jeju Island (red circle in Fig. 1, 32.983°N, 126.392°E) on 09 AM in 1 May 2016. The Community Multiscale Air Quality (CMAQ) modelling system data indicated that the NO_2 VCD from the surface to 50 hPa at this point on this day was 6.75×10^{15} molecules cm^{-2} (averaged NO_2 VCD obtained from OMI available during KOURS-AQ period is 4.77×10^{15} molecules cm^{-2} and standard deviation of 1.33×10^{15} molecules cm^{-2}, respectively); ρ_j represents the SCD of each species j; $\sigma'_j(\lambda)$ represents the differential gas phase absorption cross-section convolved with the Gaussian distribution function (GDF) with GeoTASO FWHM (the UV and VIS range were 0.34−0.49 nm and 0.70−1.00 nm, respectively (Nowlan et al., 2016)) at wavelength λ of

187 species j, respectively. The spectral fitting window was selected from 425 to 450 nm. To determine the wavelength registration
188 more accurately in the narrow fitting window, additional wavelength calibration of the spectra for each of the 33 across track
189 pixels was performed using a high-resolution solar reference spectrum (Kurucz solar spectrum) (Chance and Kurucz, 2010)
190 with the GDF. The absorption cross-sections of NO_2 (Vandaele et al., 1998), O_3 (Bogumil et al., 2000), H_2O, and the Ring
191 effect as pseudo-absorbers (Chance and Spurr, 1997) were used to construct the model equation; and $B(\lambda)$, $R(\lambda)$, $A(\lambda)$, and
192 $N(\lambda)$ are the broad absorption of the trace gases, extinction by Mie and Rayleigh scattering, variation in the spectral sensitivity
193 of the detector or spectrograph, and noise, respectively, which were accounted by an 8th order polynomial. An example of the
194 spectral fitting results is presented in Fig. 3.
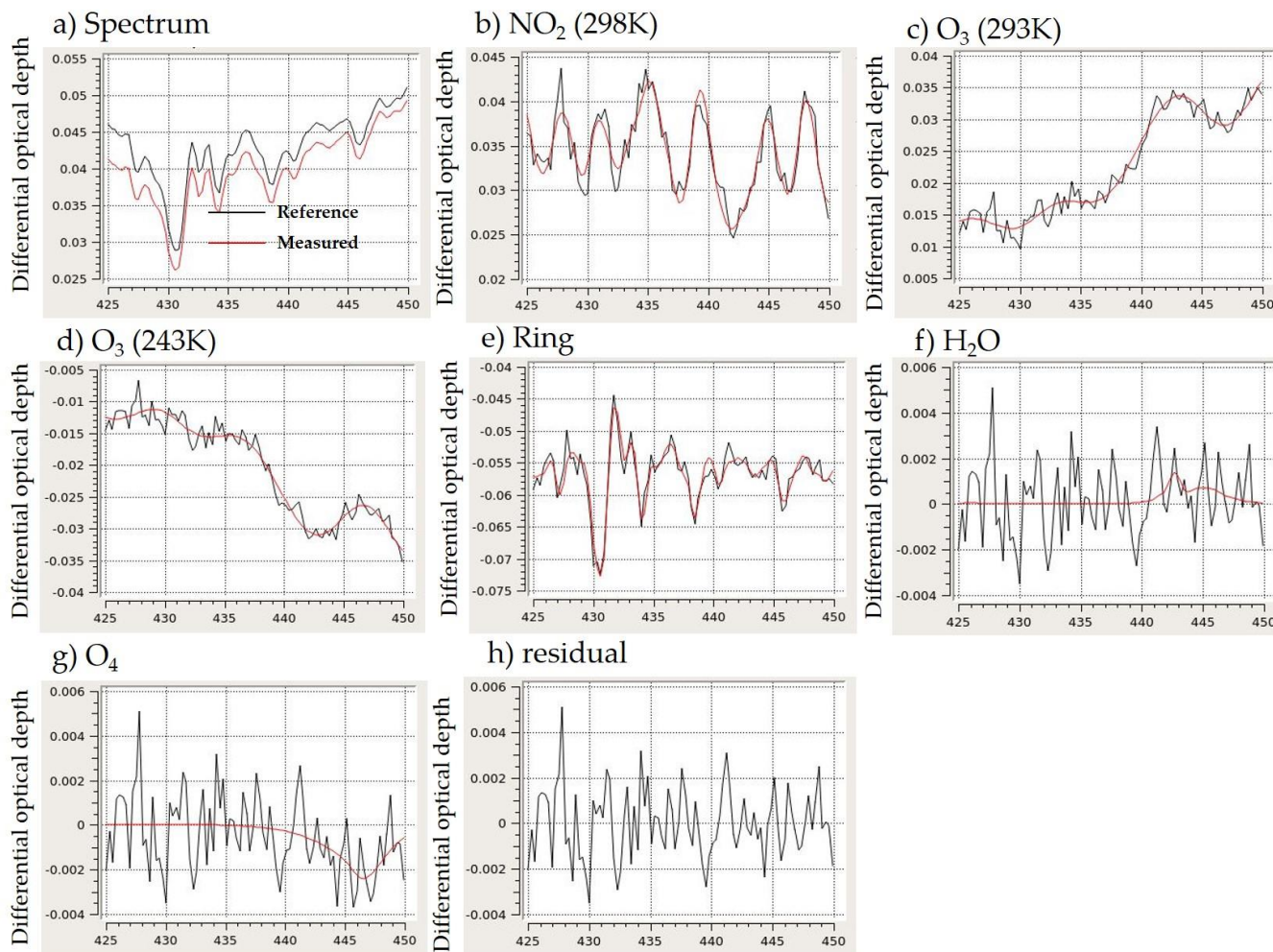
Figure 3. An example of the spectral fitting results of NO_2 retrievals from GeoTASO during the KORUS-AQ campaign (at Gangnam, Seoul on 9 June, 2016). Red and black line in the panel (a) represent measured and reference spectrum, respectively. The panels

from (b) to (h) depict examples of spectral fitting results of (b) NO₂, (c) O₃(293K), (d) O₃(243K), (e) ring, (f)H₂O, (g) O₄ where red and black lines are absorption cross section of target species and the fitting residual plus the absorption of the target species, respectively. The panel (h) shows fitting residual of this example.

2.4.2 NO₂ AMF calculation

AMF, the ratio of SCD to VCD, can be calculated using the scattering weight (ω) and shape factor (S) (Palmer et al., 2001) in Eq. (2)−(5).

$$\text{AMF} = \frac{SCD}{VCD} \tag{2}$$

$$\text{AMF} = AMF_G \int_{z1}^{z2} \omega(z)S(z)dz \tag{3}$$

$$\omega(z) = -\frac{1}{AMF_G}\frac{\partial \ln I_B}{\partial \tau} \tag{4}$$

$$S(z) = \frac{\alpha(z)n(z)}{\int_{z1}^{z2} \alpha(z)n(z)dz} \tag{5}$$

Where AMF_G represents the geometric AMF, I_B is the earthshine radiance, τ is the optical depth, α is the absorption cross-section, and n is the number density of the absorber. NO₂ AMF was calculated using a linearised pseudo-spherical scalar and vector discrete ordinate radiative transfer model (VLIDORT, version 2.6; Spurr and Christi, 2014). Aerosol properties, such as AOD, SSA, and *a priori* NO₂ vertical profile information, were simulated using the CMAQ, and surface reflectivity was obtained from the Moderate Resolution Imaging Spectroradiometer (MODIS) (Collection 6). The surface reflectance products, MOD09CMG and MYD09CMG, available at a 0.05 degree (~5.6 km) spatial resolution, provide an estimate of the surface spectral reflectance including MODIS bands 1 through 7. The products were corrected for atmospheric conditions such as aerosol, gasses, Rayleigh scattering. In previous studies (Lamsal et al., 2017; Nowlan et al., 2018; Judd et al., 2019; Chong et al., 2020), an AMF were described for both above and below aircraft altitude is used to convert NO₂ SCDs to VCDs using Eq. (6)−(8).

$$\text{AMF} \uparrow = AMF_G \int_{Z_A}^{Z_{TOA}} \omega(z)S(z)dz \tag{6}$$

$$\text{AMF} \downarrow = AMF_G \int_{Z_0}^{Z_A} \omega(z)S(z)dz \tag{7}$$

$$NO_2 \text{ VCD} \downarrow = \frac{NO_2\ SCD - AMF\uparrow \cdot NO_2VCD\uparrow}{AMF\downarrow} \tag{8}$$

Where $AMF\uparrow$ and $AMF\downarrow$ are AMF above and below aircraft, respectively, and $NO_2\ VCD\uparrow$ represents NO₂ VCD above the aircraft obtained from a chemical transport model (CTM). However, here we calculated NO₂ VCD↓ by dividing NO₂ SCDs by $AMF\downarrow$ because stratospheric and free tropospheric NO₂ ($NO_2\ VCD\uparrow$) column densities are much lower than tropospheric NO₂ column densities, especially in megacities and industrial areas (Valks et al., 2011).

2.5 Chemical model description

Vertical profiles from CMAQ (Byun and Ching, 1999; Byun and Schere, 2006), a CTM, were used to calculate AMFs. CMAQ simulations were conducted with a horizontal resolution of 15×15 km and had 27 vertical layers from the surface to 50 hPa. The meteorological fields were prepared using the advanced research Weather Research and Forecasting (WRF)-Advanced Research WRF (ARW) Model (Skamarock et al., 2008). Anthropogenic emissions were generated based on the KORUS v5.0 model (Woo et al., 2012), and biogenic emissions were simulated using the Model of Emissions of Gases and Aerosols from Nature (MEGAN v2.1; Guenther et al., 2006; 2012). Besides anthropogenic and biogenic emissions, the Fire Inventory from NCAR (FINN; Wiedinmyer et al., 2006, 2011) was utilised to update the pyrogenic emission fields. CMAQ AOD was calculated by integrating the aerosol extinction coefficient (Q_{ext}), which is the sum of scattering (Q_{sca}) and absorption (Q_{abs}) coefficients, over all vertical layers (z) as follows:

$$AOD = \int Q_{sca}(z) \, dz = \int \{Q_{sca}(z) + Q_{abs}(z) \} \, dz \tag{9}$$

$$Q_{abs}[\text{Mm}^{-1}] = \sum_i \sum_j \{(1 - \omega_{ij}) \cdot \beta_{ij} \cdot f_{ij}(RH) \cdot [C]_{ij} \} \tag{10}$$

$$Q_{sca}[\text{Mm}^{-1}] = \sum_i \sum_j \{\omega_{ij} \cdot \beta_{ij} \cdot f_{ij}(RH) \cdot [C]_{ij} \} \tag{11}$$

Here, ω_{ij} indicates SSA of particulate species i for the particulate mode (or size bin) j, β_{ij} denotes the mass extinction efficiency, $f_{ij}(RH)$ is the hygroscopicity factor according to the relative humidity (RH), and $[C]_{ij}$ is the concentration of particulate species. CMAQ SSA is defined as the ratio of the integrated Q_{sca} to AOD, and NO$_2$ vertical profiles were obtained from NO$_2$ concentrations at each vertical layers by conducting CMAQ simulations. Details of the model descriptions and calculations of optical properties are given in Lee et al. (2020) and Malm and Hand (2007).

3 Results and discussion

3.1 NO₂ VCD retrieval

We showed the finally NO$_2$ VCDs by binning them with $0.01° \times 0.01°$ from 250 m spatial resolution. Although the spatial binning NO$_2$ VCDs were compared to those at native resolution, we noted that the spatiotemporal variability was still able to be clearly distinguished from the background at $0.01°$ binning resolution. Chong et al. (2020) showed that larger VCDs at 250 m resolutions do not necessarily lead to larger VCDs at wider resolutions. As the results of NO$_2$ VCD, we selected the dates observed in both the morning and afternoon during the KORUS-AQ period over Seoul metropolitan area, Busan, and Anmyeon. The retrieved dates for NO$_2$ VCDs were 5, 9, and 10 Jun, 2016.

3.1.1 Seoul metropolitan region

The population of the Seoul metropolitan region is approximately 20 million, which is approximately 40% of the total population of South Korea. It is very rare to obtain high-resolution horizontal NO$_2$ VCD distributions using airborne

258   measurements in the morning and afternoon, especially in Asian megacities. Fig. 4 shows tropospheric NO₂ VCDs over Seoul

259   on 9 June 2016, at 9 AM and 3 PM local time (LT). According to the Terra/Aqua CLDMASK data (Ackerman et al., 1998),

260   on this day, the cloud fraction was less than 0.3 over the entire domain of Fig. 4.
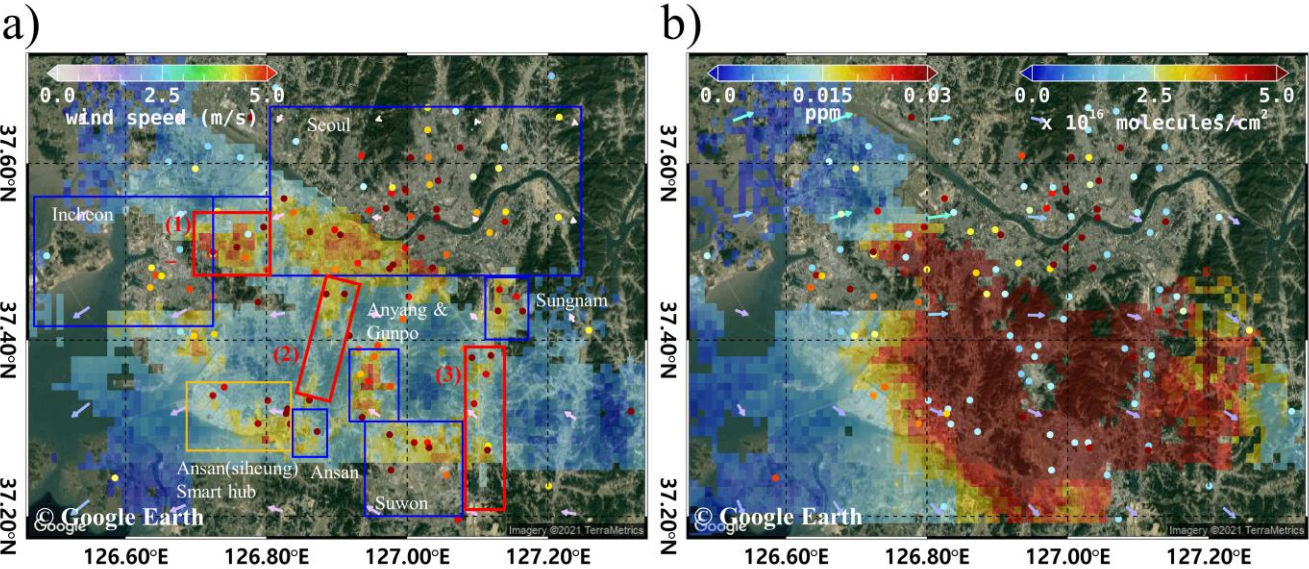
261
262   **Figure 4. Tropospheric NO₂ VCD, binned to a 0.01°×0.01° horizontal grid, in the Seoul metropolitan region on 9, June 2016 retrieved**
263   **from GeoTASO: a) at 9 AM and b) at 3 PM. The red boxes represent expressways (counterclockwise from left to right, (1) Gyeongin**
264   **expressway, (2) Seohaean expressway, and (3) Gyeongbu expressway), the orange box indicates the industrial complex, and the blue**
265   **boxes indicate the major cities (Seoul, Incheon, Suwon, Bucheon, Anyang, Gunpo, Sungnam, and Ansan) of the Seoul metropolitan**
266   **region. Colours of the circles depict the NO₂ surface mixing ratio obtained from Air-Korea. The colour arrows show the wind**
267   **direction and speed at 1000 hPa over Seoul metropolitan region, obtained via the Unified Model (UM) simulations (background**
268   **RGB image is from Google Earth; https://www.google.com/maps/).**

269

270   In the morning, NO₂ VCDs retrieved from GeoTASO were highly correlated with expressways (red boxes in Fig. 4), such as

271   the Gyeongin, Seohaean, and Gyeongbu Expressways, and over major cities with heavy traffic, such as Seoul, Bucheon, Ansan,

272   Anyang, and Suwon. GeoTASO observed NO₂ VCD values three-times higher ($>3 \times 10^{16}$ molecules cm^{-2}) in these areas

273   compared to the surrounding rural areas. In particular, high NO₂ VCD values above 6×10^{16} molecules cm^{-2} were observed

274   above the Gyeongin Expressway, which has very heavy traffic in a relatively short section, and the Gunpo Complex Logistics

275   zone, where diesel vehicle traffic is also high. The major NO₂ source regions and the regions where high NO₂ VCD values

276   were observed were highly consistent at 9 AM because the wind speed at this time—as obtained from the unified model (UM)

277   based Regional Data Assimilation and Prediction System (RDAPS) of the Korea Meteorological Administration (KMA)—

278   was as low as 0.1 ms^{-1} and the average wind direction was 84.7° at 1000 hPa over Seoul metropolitan region. The average

279   daily traffic volume of these expressways exceeds 150,000 vehicles, and the total number of vehicles registered in these major

280   cities is > 6,000,000, with an average daily mileage per car per day of over 38 km. Detailed information on these cities and

11

281 expressways is listed in Table 2 and Table 3. Based on the level of vehicular traffic, combustion using gasoline and diesel

282 engines leads to high overall emissions of NO_2 in the Seoul metropolitan region (Kendrick et al., 2015).

283

284 **Table 2. The population, number of registered vehicles, and average mileage per car per day of major cities in the Seoul**
285 **metropolitan region obtained from the Korean Statistical Information Service (https://kosis.kr/eng).**

| City	Population (millions)	Vehicle registration number (thousands)	Average mileage (km/car/day)
Seoul	9.776	3,083	37.1
Incheon	2.914	1,402	41.7
Bucheon	0.848	284	37.2
Ansan	0.744	289	40.8
Anyang	0.596	206	39.6
Gunpo	0.286	87	38.8
Suwon	1.241	467	38.1
Sungnam	0.994	358	36.3

286

287 **Table 3. Daily average traffic volume on the Gyeongin, Gyeongbu, and Seohaean Expressways obtained using the Traffic**
288 **Monitoring System (https://www.road.re.kr).**

Expressway	Daily average traffic volume
Gyeongin Expressway	162,369
Gyeongbu Expressway	173,413
Seohaean Expressway	150,298

289

290 Compared the data from the morning, the average wind speed and wind direction were 1.7 m/s and 284.5° at 1000 hPa in the

291 afternoon and the afternoon had extremely high tropospheric NO_2 VCD values (exceeding 5×10^{16} molecules cm^{-2}) in most of

292 the Seoul metropolitan regions including rural areas, whereas the NO_2 mixing ratio (MR) obtained from Air-Korea decreases

293 in the afternoon. According to Tzortziou et al. (2018), similar results were retrieved from the Pandora site in Seoul, with higher

294 afternoon NO_2 VCDs than in the morning. This result is presumed to be due to the reason that the amount of NO_2 produced by

295 chemical conversion of nitric oxide (NO) by O_3 and VOCs in the atmosphere, along with NOx generated by regional emissions

296 (traffic) in the Seoul metropolitan region, is greater than the amount lost by photolysis and transport to nearby areas (Herman

297 et al., 2018). In addition, the increase in tropospheric NO_2 VCD in the afternoon is presumed to be due to the accumulation
298 and dispersion of NO_2 according to the change in the planetary boundary layer height (Ma et al., 2013).

299 **3.1.2 Industrial and power plant regions in Anmyeon**
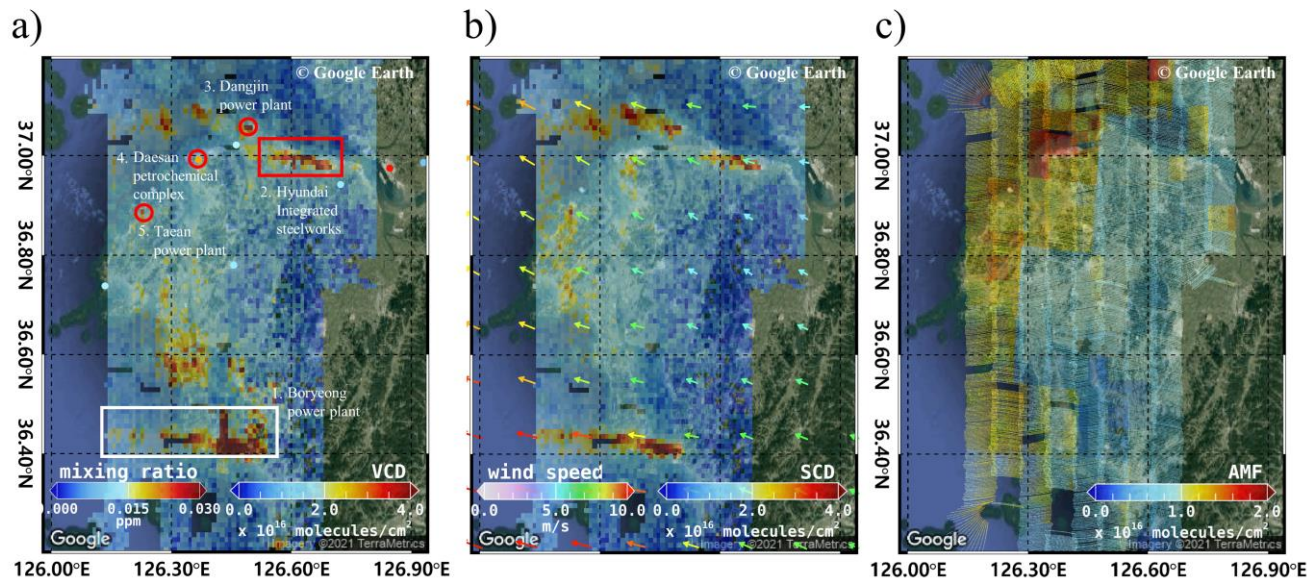
300
301 **Figure 5. a) Tropospheric NO_2 VCD and b) NO_2 SCD retrieved from GeoTASO, and c) NO_2 AMF, native resolution (250 m)**
302 **calculated using VLIDORT over Anmyeon in South Korea on 5 June 2016. The NO_2 VCD and SCD were gridded into to a spatial**
303 **resolution of 0.01°×0.01°. The colored arrows indicate wind speed and wind direction at 850 hPa from the Unified Model (UM)**
304 **simulations. The red circles and rectangle in panel (a) represent the major NO_2 emission sources, such as steelworks and power**
305 **plants (background RGB image is from Google Earth; https://www.google.com/maps/).**

306
307 The high spatial resolution of tropospheric NO_2 VCD from GeoTASO over the Anmyeon industrial region, where many
308 industrial facilities and several power plants are distributed, is shown in Fig. 5. The panels a and b of this figure show the
309 binned tropospheric NO_2 VCD and NO_2 SCD retrieved from GeoTASO L1B data, respectively, between 13:00 and 17:00 LT
310 on 5 June 2016. The panel c depicts the calculated AMF of NO_2 from native resolution over the domain. The GeoTASO
311 observations clearly detected moderate and strong NO_2 emission sources over this area: (1) Boryeong power plant, (2) the
312 Hyundai integrated steelworks, (3) Dangjin power plant, (4) the Daesan Petrochemical Complex, and (5) Taean power plant.
313 High NO_2 VCD values ($> 5 \times 10^{16}$ molecules cm^{-2}) were observed over steel mill works, petrochemical complexes, and power
314 plants, whereas values were comparatively low ($<1 \times 10^{16}$ molecules cm^{-2}) over small cities including Seosan, Dangjin, and
315 Boryeong with populations of less than 0.1 million, and the Seohaean Expressway. In 2016, the annual NOx emissions by the
316 Hyundai steelworks and the Dangjin and Boryeong power plants were about 10.3, 11.9, and 16.8 kt year^{-1}, respectively. NO_2
317 emission rates from major industrial facilities in the Anmyeon region are shown in Table 4.

318

Table 4. NO₂ emission rates from major industrial facilities in the Anmyeon region obtained from the Continuous Emission Monitoring System of the Korea Environment Corporation (https://www.stacknsky.or.kr/eng/index.html).

Industrial facilities	NO$_2$ emission rate (2016) (kg/year)
Boryeong power plant	16,788,438
Hyundai integrated steelworks	10,271,075
Dangjin power plant	11,852,972
Daesan petrochemical complex	3,397,939
Taean power plant	15,466,022

321

322 Figure 5 shows high NO_2 concentrations of major industrial facilities in the Anmyeon region, where fossil fuel combustion in

323 factories and thermal power plants leads to high emissions (Prasad et al., 2012). Due to relatively sparse distribution over rural

324 areas, the Air-Korea measurements did not detect the major NO_2 plume as shown in Fig. 5a. Thus, airborne remote sensing

325 systems, such as GeoTASO, can effectively compliment the ground-based networks for monitoring minor and major NO_2

326 emissions, particularly over these remote industrial regions.


327
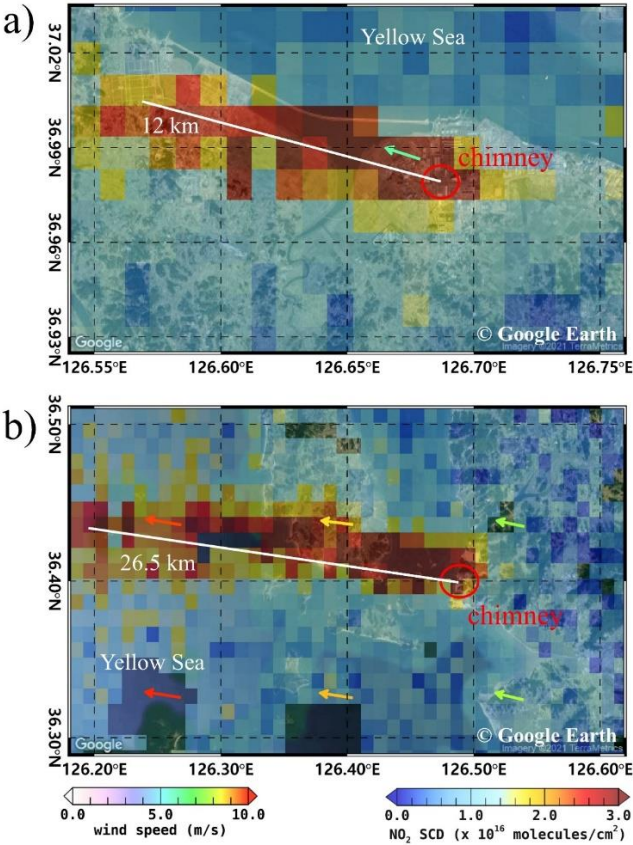
Figure 6. Enlarged view of GeoTASO tropospheric NO_2 VCD observation over a) Hyundai steel works, indicated by the red box in Figure 5, and b) the Boryeong power plant, indicated by the white box in Figure 5. The data were gridded to a spatial resolution of 0.01°×0.01°. The arrows represent the wind direction and speed at 850 hPa from the Unified Model (UM) simulations, respectively (background RGB image is from Google Earth; https://www.google.com/maps/).

332

333 The GeoTASO data captured not only NO_2 emissions from the chimneys of steelworks and power plants but also its transport

334 by the wind. Fig. 6a and 6b show enlarged views of tropospheric NO_2 SCD retrieved using GeoTASO over the Hyundai

335 steelworks (red box in Fig. 5) and the Boryeong power plant (white box in Fig. 5). The arrows in Fig. 6 represent the prevailing

336 wind direction and speed from RDAPS. NO_2 emitted from the chimneys of these sites was transported to the Yellow Sea,

15

337 travelling distances of over 26 km at speeds of approximately 6 ms^{-1}. According to Chong et al. (2020), similar results were

338 found for SO$_2$ emitted and transported from these sites.

3.1.3 Busan metropolitan region

340
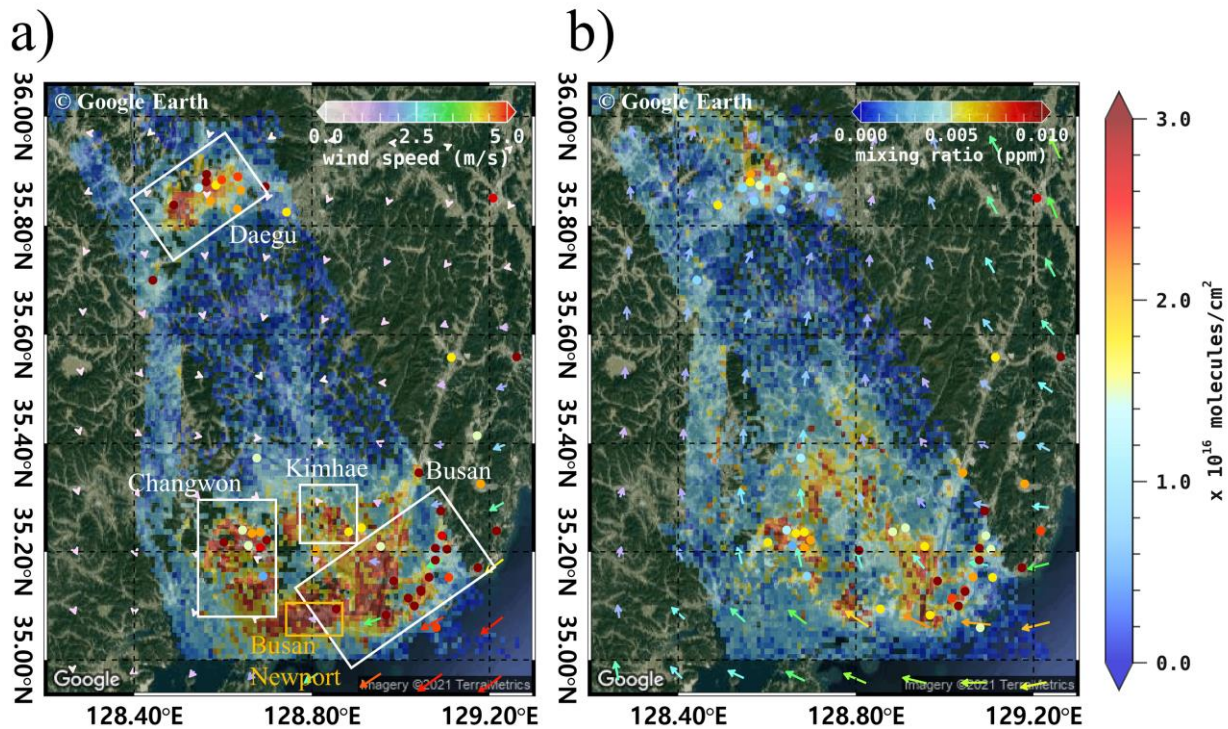
Figure 7. Tropospheric NO$_2$ VCD in the Busan metropolitan region in the (a) morning and (b) afternoon of 10 June 2016. The data were gridded into to a spatial resolution of 0.01°×0.01°. The wind speed (colours scale) and wind direction (arrows) at 1000 hPa pressure level were obtained from the Unified Model (UM) simulations. The white boxes represent major cities such as Busan, Daegu, Changwon, and Kimhae. The orange box represents Busan Newport (background RGB image is from Google Earth; https://www.google.com/maps/).

346

347 Fig. 7a and 7b show tropospheric NO$_2$ VCD retrieved from the GeoTASO L1B data over the Busan metropolitan region on 10

348 June 2016 in the morning (between 08:00 and 11:00 LT) and afternoon (between 13:00 and 16:00 LT), respectively. The

349 arrows in Fig. 7 show the wind speed and wind direction of 1000 hPa obtained from the UM-RDAPS, with the average wind

350 speed and wind direction of 0.9 m/s and 55.4°, 1.9 m/s and 147.0°, respectively, in the morning and afternoon. High NO$_2$

351 VCDs were observed above urban areas, the port, industrial complexes, and the inter-city road between Busan and Changwon.

352 Similar to the Seoul metropolitan regions, it is estimated that combustion using gasoline and diesel engines contributes to the

353 high NO$_2$ emission. In the morning, NO$_2$ VCDs were high (approximately 3×10^{16} molecules cm^{-2}) in the major cities and,

354 especially, around Busan Newport, with values exceeding 7×10^{16} molecules cm^{-2}. In comparison, in the mountainous regions

16

355 between Daegu and Busan, NO$_2$ VCD values were less than 1×10^{16} molecules cm^{-2} during the same period. The spatial

356 distribution of tropospheric NO$_2$ VCDs was similar to that in the Seoul metropolitan regions, with high values over major cities

357 and roads (compare Figs. 4 and 7). In Busan, fossil fuel combustion using both road vehicles and ships likely contributes to

358 the NO$_2$ emissions. In the afternoon, unlike Seoul metropolitan region, tropospheric NO$_2$ VCD over Busan decreased by over

359 3×10^{16} molecules cm^{-2}, which also corresponds with NO$_2$ MR data obtained from the Air-Korea sites. Detailed information

360 on these cities is listed in Table 5.

361

362 **Table 5. The population, number of registered vehicles, and average mileage per car per day of major cities in the Busan**
363 **metropolitan region obtained from the Korean Statistical Information Service (https://kosis.kr/eng).**

City	Population (millions)	Vehicle registration number (thousands)	Average mileage (km/car/day)
Busan	3.389	1,295	40.1
Daegu	2.450	1,121	37.1
Changwon	1.080	551	37.5
Kimhae	0.529	250	38.0

364

365 **3.2 Error estimation**

366 NO$_2$ VCD retrieval accuracy using the DOAS method depends on both the AMF calculation and spectral fitting error of the

367 SCD retrieval. Retrieval errors of the NO$_2$ VCD were estimated using error propagation analysis as expressed in Eq. (12).

368 $$\frac{\varepsilon_{VCD}}{VCD} = \sqrt{\left(\frac{\varepsilon_{SCD}}{SCD}\right)^2 + \left(\frac{\varepsilon_{AMF}}{AMF}\right)^2} \qquad (12)$$

369 Where ε_{VCD} is the total error of NO$_2$ VCD. The error of NO$_2$ SCD (ε_{SCD}) is obtained from the spectral fitting error of NO$_2$ SCD

370 via DOAS spectral fitting. ε_{AMF} indicates the error of NO$_2$ AMF caused by uncertainties in the model input parameters for

371 AMF calculation. Uncertainties in aerosol properties (AOD, SSA, and ALH) and surface reflectance for the RTM calculations

372 are known to be the major factors affecting NO$_2$ AMF accuracy (Boersma et al., 2004; Leitão et al., 2010; Hong et al., 2017).

373 Therefore, in this present study, we quantified the NO$_2$ AMF errors (ε_{AMF}) due to uncertainties in the input parameters

374 independent of one another using Eq. (13):

375 $$\varepsilon_{AMF} = \sqrt{\left(\frac{\partial AMF}{\partial AOD}\right)^2 \sigma AOD^2 + \left(\frac{\partial AMF}{\partial SSA}\right)^2 \sigma SSA^2 + \left(\frac{\partial AMF}{\partial ALH}\right)^2 \sigma ALH^2 + \left(\frac{\partial AMF}{\partial SFR}\right)^2 \sigma SFR^2} = \sqrt{\sum_{i=1}^{4}\left(\frac{\partial AMF}{\partial \chi_i}\right)^2 \sigma_{\chi_i}^2}, \qquad (13)$$

376 where $\frac{\partial AMF}{\partial \chi_i}$ are partial derivatives of NO$_2$ AMF with respect to the input parameters (χ_i), σ_{χ_i} represents the uncertainty of the

377 χ_i. The σ of AOD, SSA, surface reflectance, and ALH are assumed as 30% (Ahn et al., 2014), 0.04 (Jethva et al., 2014),

378 (0.005+0.05×surface reflectance; EOS Land Validation; https://landval.gsfc.nasa.gov), and 1 km (Fishman et al., 2012),

17

379 respectively, in this study. To derive $(\frac{\partial AMF}{\partial \chi_i})^2$, the true χ_i is input to the RTM to simulate 'true' NO$_2$ AMF. For the AOD, SSA,

380 ALH, and surface reflectance (SFR), perturbed NO$_2$ AMF was simulated using RTM with $\chi_i \pm \sigma\chi_i$. $\partial\chi_i$ denotes the difference

381 between the 'true' χ_i and $\chi_i \pm \sigma\chi_i$, and ∂AMF is the difference between the 'true' NO$_2$ AMF (AMF$_{true}$) simulated with 'true'

382 input values and the new NO$_2$ AMF (AMF$_{new}$) simulated using the perturbed input parameters $\chi_i \pm \sigma\chi_i$ (i.e. the original input

383 parameters modified by the uncertainty). The simulation for calculating the ε_{AMF} was conducted using the input parameters

384 on 9 June 2016. On the flight day, average (standard deviation) values of AOD, SSA, ALH, and surface reflectance were 0.39

385 (0.10), 0.98 (0.001), 0.27 km (0.10 km), and 0.09 (0.04), respectively.

386

387 **Table 6. Total errors of NO$_2$ VCD caused by uncertainties in NO$_2$ SCD and NO$_2$ AMF (the average for the flight on 9 June**

388 **2016).**

	AOD	3.0%
	SSA	4.2%
NO$_2$ AMF **errors**	aerosol loading height	26.4%
	surface reflectance	2.8%
	total NO$_2$ AMF error **due to aerosol uncertainties**	**27.8%**
	NO$_2$ SCD error	**11.9%**
	NO$_2$ VCD error	**31.1%**

389

390 Table 6 lists the estimated NO$_2$ VCD error on 9 June 2016 for each sources based on the error propagation method. The error

391 estimation was conducted for the pixels where root mean square residual < 0.001 and NO$_2$ VCD > 5×10^{15} molecules cm^{-2}

392 since NO$_2$ SCD precision is reported to be highly decreased in low NO$_2$ conditions (Hong et al., 2017). The total NO$_2$ VCD

393 error was 31.1% with a high portion of NO$_2$ AMF error. The NO$_2$ SCD error was calculated to be 11.9%, showing the

394 importance of accurate DOAS spectral fitting to derive NO$_2$ SCD. The total AMF error due to uncertainties in input parameters

395 was calculated to be 27.8%. Among model input parameters, the effect of ALH on NO$_2$ AMF become highest (26.4%),

396 indicating importance of accurate aerosol profile information. ALH sensitively affects NO$_2$ AMF because near the surface

397 where trace gases and aerosols are well mixed, aerosols lead to multiple scattering effects and the light absorption of trace

398 gases due to increasing light path (Castellanos et al., 2015; Hong et al., 2017). Especially, ALH can be the most important

399 input parameter in the Asia region where high loadings of aerosol plumes persist throughout the year. The NO$_2$ AMF

400   calculation errors due to uncertainties in SSA and AOD were 4.2% and 3.0%, respectively. The NO_2 AMF calculation error

401   due to uncertainties in aerosol optical properties (SSA and AOD) seems smaller than those in the previous study (Leitão et al.,

402   2010). The smaller effect of aerosol properties can be explained by the moderate aerosol loading (AOD = 0.39) on the flight

403   day. It is expected that NO_2 AMF errors become larger under high AOD condition. The smallest effect of SRF was found on

404   NO_2 AMF calculation error. A priori NO_2 profile shape also can be one of factors to cause calculation error for NO_2 AMF as

405   reported in the previous studies (Leitao et al., 2010, Meier et al., 2016). It is necessary to calculate the effect of a priori NO_2

406   profile shape on airborne NO_2 AMF error in the future. Moreover, the resulting uncertainties of input parameters of a

407   GeoTASO ground pixel need to be considered by combining the initial uncertainties of CTM and satellite-based products, and

408   by the variability of the parameters within a grid box. This kind of analysis should be taken into account in further study.

409      $$AMF_{percent\_diff} = \frac{\partial AMF}{(AMF_{true} + AMF_{new}) \div 2} \times 100 \tag{14}$$

410
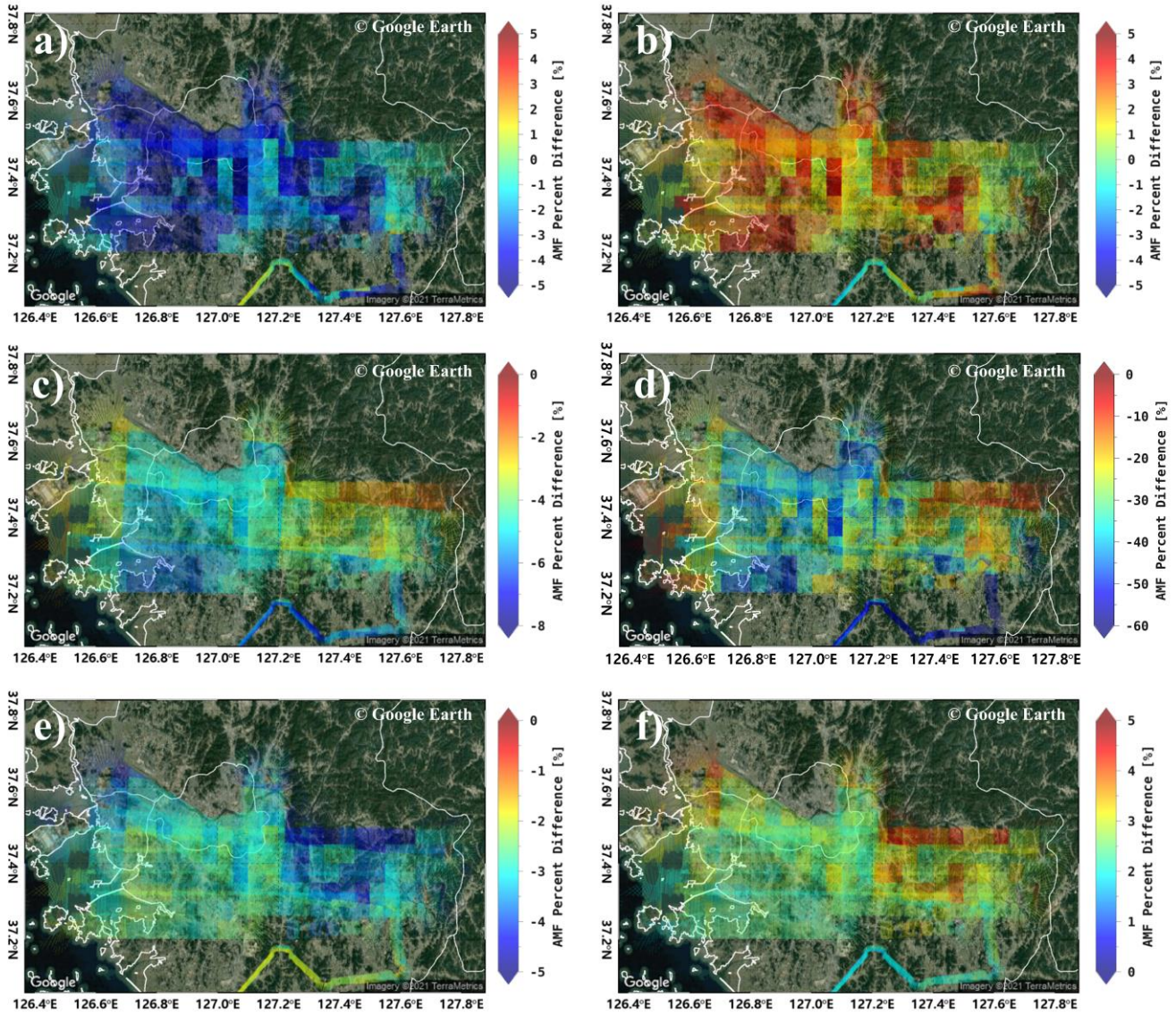
Figure 8. Percentage difference between AMF calculated using the CMAQ model simulation and those using a) 30% lower AOD, b) 30% higher AOD, c) 0.04 lower SSA, d) 1km higher ALH, compared to the model outputs. The percentage difference for AMF calculated using MODIS data and those using e) 20% 0.005 + 0.05 × SFR lower SFR, f) 0.005 + 0.05 × SFR higher SFR (background RGB image is from Google Earth; https://www.google.com/maps/).

In this present study, we additionally investigated the spatial distribution of AMF calculation errors associated with uncertainties in aerosol properties (AOD, SSA, ALH, and SFR). Percent difference of NO_2 AMF ($AMF_{percent\_diff}$) was calculated on each spatial pixel using Eq. (14). Fig. 8a and 8b show the percent difference error between the calculated AMFs using the

20

CMAQ AOD data with 30% lower (Fig. 8a) and 30% higher (Fig. 8b) values, respectively. The AMF decreased and increase by up to 7% with decreasing and increasing AOD, respectively, in the Seoul metropolitan region. We estimated that, under low aerosol loading conditions, an increase in AOD near the surface leads to an increase in the scattering probability within the surface layer with high NO_2 concentrations. Fig. 8c shows the percent difference error between the calculated AMFs using CMAQ SSA data with a 0.04 lower value. The AMF decreased with decreasing SSA because the absorption of light increased. The ALH was also found to highly affect the accuracy of the AMF calculations (Fig. 8d). The ALH uncertainty of 1 km decreased AMFs with average $AMF_{percent\_diff}$ of -27% on the flight day. Especially, on the pixels where AOD > 0.6, the average $AMF_{percent\_diff}$ was found to be -37% while that was -23% on the pixels where AOD < 0.4, showing the combined effect of aerosol loading and aerosol profile shape on the NO_2 AMF calculations. Fig. 8e and 8f show the percentage difference error between the calculated AMFs using the MODIS surface reflectance data with $0.005 + 0.05 \times SFR$ lower (Fig. 8e) and $0.005 + 0.05 \times SFR$ higher (Fig. 8f) values, respectively. The AMF decreased by about 6% when surface reflectance decrease, and vice versa when it increased.

3.3 Validation of NO_2 VCDs retrieved from GeoTASO

Tropospheric NO_2 VCDs retrieved from GeoTASO L1B data ($NO_{2,G}$) were compared with those obtained from OMI NO_2 VCDs ($NO_{2,O}$) and Pandora ($NO_{2,P}$). The $NO_{2,O}$ were only available for 10 June during the campaign period. Therefore, we only compared 37 $NO_{2,G}$ and $NO_{2,O}$ data points within a radius of 20 km and 30 min, which yielded a correlation coefficient of 0.70 with a slope of 0.41 (Fig. 9 a)). In order to validate, All $NO_{2,G}$ within a radius 20 km of the OMI center coordinate were averaged.

The NO_2 values are relatively low since GeoTAOS observation is carried out in a region with low NO_2 compared to Seoul metropolitan and the overpass time of OMI is about 13:30 LT when NO_2 decreased. It is thought that the reson the low slope value is because the OMI with low spatial resolution does not reflect the spatial NO_2 inhomogeneity in the pixel.
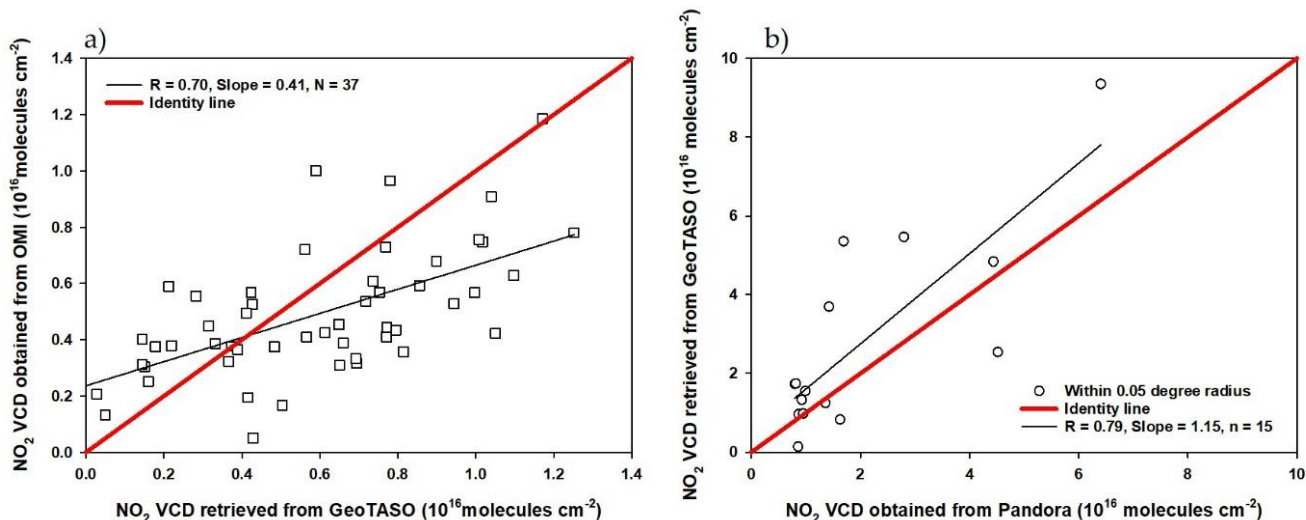
Figure 9. Scatter plots of a) NO₂ VCD retrieved from GeoTASO and those obtained from OMI and b) NO₂ VCD obtained from Pandora and those retrieved from GeoTAOS, respectively.

To validate the accuracy of $NO_{2,G}$ data, we made a comparison with NO_2 VCD obtained from the Pandora system ($NO_{2,P}$) during the KORUS-AQ campaign period. $NO_{2,P}$ obtained from Busan University, Olympic Park, Songchon, Yeoju, and Yonsei University Pandora sites on June 5, 9, and 10 were used for the GeoTASO validation (Fig. 1). $NO_{2,G}$ and $NO_{2,P}$ columns at these sites are compared in Fig. 10. In order to compare $NO_{2,G}$ and $NO_{2,P}$, we used averaged $NO_{2,G}$ retrieved from 16 across track with smallest viewing zenith angle and averaged 30 min NO_2 obtained from pandora measurement within a radius of 0.05 degree. $NO_{2,G}$ and $NO_{2,P}$ were correlated (R = 0.79, with a slope of 1.15), however, when $NO_{2,P}$ was lower than 1×10^{16} molecules cm^{-2}, the correlation coefficient between $NO_{2,G}$ and $NO_{2,P}$ was < 0.1. The weak correlation at low NO_2 levels are most likely to reflect the differences in viewing geometries and the horizontal inhomogeneity of the measured NO_2 between Pandora and GeoTASO. Also, from this result, it is thought that it can be used for NO_2 validation of geostationary satellite such as GEMS using Pandora and GeoTASO. However, since the number of pandora is limited in this campaign, we had difficulties to validate NO_2 retrieved from GeoTASO under various conditions. I believe that many ground-based remote sensing measurements are needed to validate GEMS under various conditions.
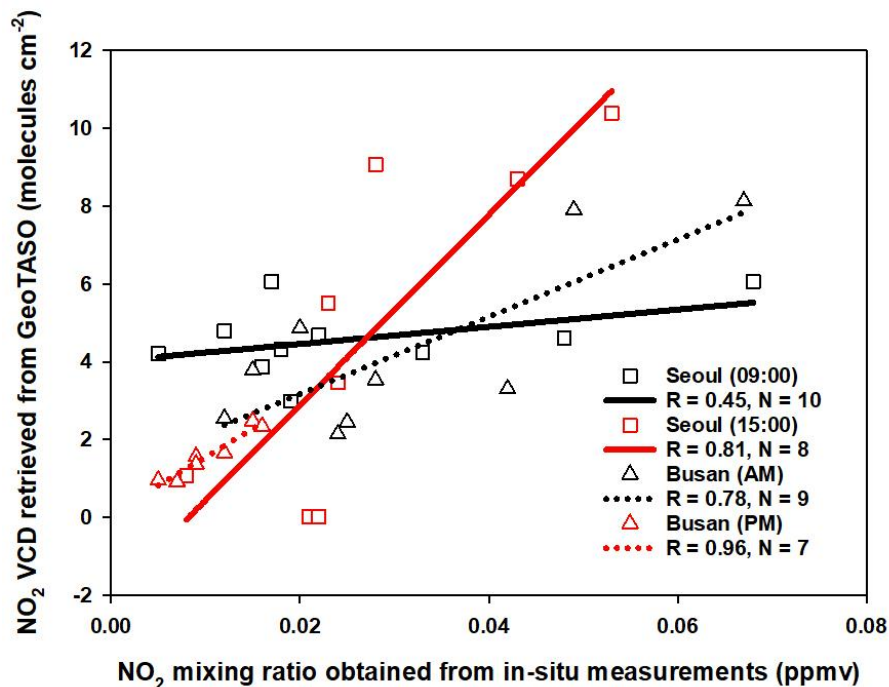
Figure 10. Scatter plot of the NO$_2$ VCDs retrieved from GeoTASO, and NO$_2$ surface mixing ratio obtained from Air-Korea. The black and red squares represent the NO$_2$ data at 9 AM and 3 PM (local time) over the Seoul metropolitan region, respectively. The black and red triangles represent those in the morning and afternoon, over Busan, respectively.

To evaluate the spatiotemporal distribution of NO$_2$ VCDs retrieved from GeoTASO, NO$_{2,G}$ in comparisons to surface spatial patterns, NO$_{2,G}$ was compared with NO$_{2,A}$ for GeoTASO data within a radius of approximately 0.05 km and 30 min (Fig. 9). In order to compare NO$_{2,G}$ and NO$_{2,A}$, we used averaged NO$_{2,G}$ retrieved from 16 across track and averaged 30 min within a radius of 0.05 degree. Since in-situ measurements provides NO$_2$ VMR (NO$_{2,A}$)(ppmv) once per hour, NO$_{2,A}$ of the nearest time is used to compare with NO$_{2,G}$. The correlation coefficient (R) between NO$_{2,G}$ (molecules cm^{-2}) and NO$_{2,A}$ at 9 AM and 3 PM LT in the Seoul metropolitan region was 0.45 and 0.81, respectively. When using only roadside station data from Air-Korea, the R-value for the morning increased to 0.83, which implies GeoTASO is more sensitive to emissions from NO$_2$ source areas, such as roadsides. As a result of the comparison, there were large differences in the morning and afternoon. These results were identified because synoptic meteorology played an important role from June 1 to June 10, 2016 (Choi et al., 2019). As described by Judd et al. (2018), the spatial distribution for NO$_2$ VCDs appears that reflects the emission source in local industrialized regions and transportations in the morning with relatively weak winds. In general, NO$_2$ concentration increases to late morning, indicating that the emissions process proceeds faster than the NO$_2$ removal process. As the planetary boundary layer heights (PBLH) in early afternoon increase and surface NO$_2$ is mixed through a deeper PBLH, the NO$_2$ VCDs distribution showed a wider increase in most of the Seoul metropolitan area and the overall column amounts continue to increase (Judd et al., 2018).

23

480   In addition, when comparing NO_2 VCDs with surface NO_2 concentrations, it should be interpreted carefully that it is a non-

481   linear relationship between $NO_{2,G}$ and $NO_{2,A}$. Although it may vary depending on weather conditions, high NO_2 VCDs from

482   airborne observations may sometimes be detected with low surface NO_2 concentrations. In particular, when exhaust gases

483   emitted from industrial facilities are happen at a certain altitude (stacks/chimneys), $NO_{2,G}$ show high NO_2 VCDs, but $NO_{2,A}$

484   may be observed to have a low concentration. Unfortunately, in Anmyeon industrial region, $NO_{2,G}$ and $NO_{2,A}$ could not be

485   compared due to spatial restrictions because the distribution of ground observation stations is concentrated in metropolitan

486   areas.

487   In the Busan metropolitan area, the R-value of the $NO_{2,G}$ and $NO_{2,A}$ data had a correlation coefficient greater than 0.78. This

488   reflects the more even horizontal distribution of NO_2 in the afternoon, when diffusion from the source areas had taken place.

489   However, for a more accurate comparison, NO_2 VCD data should be converted to NO_2 MR based on mixing layer height,

490   temperature, and pressure profile data (Kim et al., 2017; Qin et al., 2017; Jeong and Hong, 2021a). However, since the number

491   of pandora and satellite data is limited in this campaign, we had difficulties to validate NO_2 retrieved from GeoTASO under

492   various conditions. Since ground-based, airborne and space borne remote sensing measurements has their own advantage and

493   disadvantage, I believe that a comprehensive observation campaign involving all of groud-based, airborne and space borne

494   measurements should be carried out continuously for upcoming new era of geostationary environmental satellite.

495   4 Conclusions

496   For the first time, we have retrieved NO_2 VCD data using airborne GeoTASO observations over the Seoul metropolitan

497   region—one of the most populous cities worldwide, the Busan metropolitan region—the second-largest city in South Korea,

498   and Anmyeon, with thermal power plants and industrial complexes. By retrieving NO_2 data using GeoTASO L1B radiance, it

499   was possible to observe the spatial distribution of NO_2 over these metropolitan and industrial regions. In the morning,

500   tropospheric NO_2 VCD over Seoul showed a strong horizontal gradient between rural and urban areas. In urban areas,

501   tropospheric NO_2 VCD was high, with values exceeding 3×10^{16} molecules cm^{-2}; in rural areas, values were typically below

502   1×10^{16} molecules cm^{-2}. Extremely high values over 10×10^{16} molecules cm^{-2} were also observed in both rural and urban

503   areas. In Anmyeon, GeoTASO observations showed NO_2 is mainly emitted from the chimneys of industrial complexes and

504   thermal power plants, and subsequently transported by wind approximately 30 km to the Yellow Sea of the west coast of the

505   Korean Peninsula. In the Busan metropolitan region, in the morning, tropospheric NO_2 VCDs showed a similar pattern to the

506   Seoul metropolitan region, with high values above the inter-city road. However, in contrast to Seoul, tropospheric NO_2 VCDs

507   in Busan decreased in the afternoon due to different weather conditions locally.

508   To compare the data retrieved from the GeoTASO system, we compared $NO_{2,G}$ with $NO_{2,O}$ obtained from the OMI, $NO_{2,A}$

509   obtained from Air-Korea, and $NO_{2,P}$ obtained from the Pandora observation system. When the distance between two

510   observations was below 20 km or 0.05 degree within 30 min, the correlation coefficients were relatively high (R = 0.70, and

511   79, respectively). However, the correlation between $NO_{2,G}$ and $NO_{2,A}$ over the Seoul metropolitan region was weak (R = 0.45)

512   in the morning because of the more pronounced NO_2 horizontal gradient.

513   The GeoTASO system successfully observed NO_2 VCDs with a high horizontal spatial resolution for both metropolitan and

514   industrial regions. This demonstrates that airborne remote sensing measurements from GeoTASO, similar to GCAS, APEX

515   and others, can be a very effective tool for the validation of trace gases retrieved from environmental satellites, including the

516   OMI, TROPOMI, and GOME-2; these systems can obtain high-resolution measurements over relatively wide areas. However,

517   to validate geostationary environmental satellites with higher spatiotemporal resolutions, such as the GEMS, TEMPO, and

518   sentinel-4, additional validation strategies are needed. Based on error estimation, it can be concluded that aerosol properties

519   are relevant and should be determined and NO_2 vertical profile retrieval performed using, for example, LIDAR, MAX-DOAS,

520   and sondes. This is important because the accuracy of aerosol properties and the NO_2 vertical profiles affects the accuracy of

521   AMF calculations (Leitão et al., 2010; Hong et al., 2017; Lorente et al., 2017; Boersma et al., 2018). Furthermore, as we

522   observed in the Seoul metropolitan area, more closely spaced observations using ground-based remote sensing systems and in

523   situ measurements are needed as NO_2 displays large horizontal gradients, especially in the morning.

Author contributions

525   **GH** and **HH** designed and implemented the research. **KL** provided the CTM data. **GH** developed the code for model running

526   and performed the RTM simulations. **HH** and **UJ** contributed to the analysis of ground-based data. **GH** and **WC** carried out

527   the sensitivity test. **GH**, **KL**, **HH**, **UJ**, **WC,** and **JJS** revised and edited the paper. **HH** and **UJ** provided constructive comments.

528   All authors contributed to this works.

Competing interests

530   The authors declare that they have no conflict of interest.

539 **References**

540 Ackerman, S. A., Strabala, K. I., Menzel, W. P., Frey, R. A., Moeller, C. C., and Gumley, L. E.: Discriminating clear sky from
541 clouds with MODIS, J. Geophys. Res., 103, 32141–32157, https://doi.org/10.1029/1998JD200032, 1998.

542 Boersma, K. F., Eskes, H. J., and Brinksma, E. J.: Error analysis for tropospheric NO_2 retrieval from space: ERROR
543 ANALYSIS FOR TROPOSPHERIC NO_2, J. Geophys. Res., 109, n/a-n/a, https://doi.org/10.1029/2003JD003962, 2004.

544 Boersma, K. F., Eskes, H. J., Richter, A., De Smedt, I., Lorente, A., Beirle, S., van Geffen, J. H. G. M., Zara, M., Peters, E.,
545 Van Roozendael, M., Wagner, T., Maasakkers, J. D., van der A, R. J., Nightingale, J., De Rudder, A., Irie, H., Pinardi, G.,
546 Lambert, J.-C., and Compernolle, S. C.: Improving algorithms and uncertainty estimates for satellite NO_2 retrievals: results
547 from the quality assurance for the essential climate variables (QA4ECV) project, Atmos. Meas. Tech., 11, 6651–6678,
548 https://doi.org/10.5194/amt-11-6651-2018, 2018.

549 Brauer, M., Hoek, G., Van Vliet, P., Meliefste, K., Fischer, P. H., Wijga, A., Koopman, L. P., Neijens, H. J., Gerritsen, J.,
550 Kerkhof, M., Heinrich, J., Bellander, T., and Brunekreef, B.: Air Pollution from Traffic and the Development of Respiratory
551 Infections and Asthmatic and Allergic Symptoms in Children, Am J Respir Crit Care Med, 166, 1092–1098,
552 https://doi.org/10.1164/rccm.200108-007OC, 2002.

553 Burrows, J. P., Hölzle, E., Goede, A. P. H., Visser, H., and Fricke, W.: SCIAMACHY—scanning imaging absorption
554 spectrometer for atmospheric chartography, Acta Astronautica, 35, 445–451, https://doi.org/10.1016/0094-5765(94)00278-T,
555 1995.

556 Burrows, J. P., Weber, M., Buchwitz, M., Rozanov, V., Ladstätter-Weißenmayer, A., Richter, A., DeBeek, R., Hoogen, R.,
557 Bramstedt, K., Eichmann, K.-U., Eisinger, M., and Perner, D.: The Global Ozone Monitoring Experiment (GOME): Mission
558 Concept and First Scientific Results, 56, 151–175, https://doi.org/10.1175/1520-0469(1999)056<0151:TGOMEG>2.0.CO;2,
559 1999.

560 BYUN, D.: Science algorithms of the EPA Models-3 Community Multiscale Air Quality (CMAQ) Modeling System, 1999.

561 Byun, D. and Schere, K. L.: Review of the Governing Equations, Computational Algorithms, and Other Components of the
562 Models-3 Community Multiscale Air Quality (CMAQ) Modeling System, Appl. Mech. Rev., 59, 51,
563 https://doi.org/10.1115/1.2128636, 2006.

564 Callies, J., Corpaccioli, E., Eisinger, M., Hahne, A., and Lefebvre, A.: GOME-2-Metop's second-generation sensor for
565 operational ozone monitoring, ESA Bull, 1, 28–36, 2000.

566 Castellanos, P., Boersma, K. F., Torres, O., and de Haan, J. F.: OMI tropospheric NO_2 air mass factors over South America:
567 effects of biomass burning aerosols, Atmos. Meas. Tech., 8, 3831–3849, https://doi.org/10.5194/amt-8-3831-2015, 2015.

Chance, K. and Kurucz, R. L.: An improved high-resolution solar reference spectrum for earth's atmosphere measurements in the ultraviolet, visible, and near infrared, Journal of Quantitative Spectroscopy and Radiative Transfer, 111, 1289–1295, https://doi.org/10.1016/j.jqsrt.2010.01.036, 2010.

Chance, K. V. and Spurr, R. J. D.: Ring effect studies: Rayleigh scattering, including molecular parameters for rotational Raman scattering, and the Fraunhofer spectrum, Appl. Opt., 36, 5224, https://doi.org/10.1364/AO.36.005224, 1997.

Choi, S., Lamsal, L. N., Follette-Cook, M., Joiner, J., Krotkov, N. A., Swartz, W. H., Pickering, K. E., Loughner, C. P., Appel, W., Pfister, G., Saide, P. E., Cohen, R. C., Weinheimer, A. J., and Herman, J. R.: Assessment of NO_2 observations during DISCOVER-AQ and KORUS-AQ field campaigns, Atmos. Meas. Tech., 13, 2523–2546, https://doi.org/10.5194/amt-13-2523-2020, 2020.

Choi, W. J.: Introducing the geostationary environment monitoring spectrometer, J. Appl. Rem. Sens., 12, 1, https://doi.org/10.1117/1.JRS.12.044005, 2018.

Choi, M., Lim, H., Kim, J., Lee, S., Eck, T. F., Holben, B. N., Garay, M. J., Hyer, E. J., Saide, P. E., and Liu, H.: Validation, comparison, and integration of GOCI, AHI, MODIS, MISR, and VIIRS aerosol optical depth over East Asia during the 2016 KORUS-AQ campaign, Atmospheric Measurement Techniques, 12(8), 4619-4641, https://doi.org/10.5194/amt-12-4619-2019, 2019.

Chong, H., Lee, S., Kim, J., Jeong, U., Li, C., Krotkov, N. A., Nowlan, C. R., Al-Saadi, J. A., Janz, S. J., Kowalewski, M. G., Ahn, M.-H., Kang, M., Joiner, J., Haffner, D. P., Hu, L., Castellanos, P., Huey, L. G., Choi, M., Song, C. H., Han, K. M., and Koo, J.-H.: High-resolution mapping of SO2 using airborne observations from the GeoTASO instrument during the KORUS-AQ field study: PCA-based vertical column retrievals, Remote Sensing of Environment, 241, 111725, https://doi.org/10.1016/j.rse.2020.111725, 2020.

Choo, G.-H., Seo, J., Yoon, J., Kim, D.-R., and Lee, D.-W.: Analysis of long-term (2005–2018) trends in tropospheric NO_2 percentiles over Northeast Asia, Atmospheric Pollution Research, 11, 1429–1440, https://doi.org/10.1016/j.apr.2020.05.012, 2020.

Danckaert, T., Fayt, C., Van Roozendael, M., De Smedt, I., Letocart, V., Merlaud, A., and Pinardi, G.: QDOAS Software user manual, Belgian Institute for Space Aeronomy, 2016.

de Foy, B., Lu, Z., and Streets, D. G.: Satellite NO_2 retrievals suggest China has exceeded its NOx reduction goals from the twelfth Five-Year Plan, Sci Rep, 6, 35912, https://doi.org/10.1038/srep35912, 2016.

General, S., Pöhler, D., Sihler, H., Bobrowski, N., Frieß, U., Zielcke, J., Horbanski, M., Shepson, P. B., Stirm, B. H., Simpson, W. R., Weber, K., Fischer, C., and Platt, U.: The Heidelberg Airborne Imaging DOAS Instrument (HAIDI) – a novel imaging DOAS device for 2-D and 3-D imaging of trace gases and aerosols, Atmos. Meas. Tech., 7, 3459–3485, https://doi.org/10.5194/amt-7-3459-2014, 2014.

Guenther, A., Karl, T., Harley, P., Wiedinmyer, C., Palmer, P. I., and Geron, C.: Estimates of global terrestrial isoprene emissions using MEGAN (Model of Emissions of Gases and Aerosols from Nature), Atmos. Chem. Phys., 6, 3181–3210, https://doi.org/10.5194/acp-6-3181-2006, 2006.

602   Guenther, A. B., Jiang, X., Heald, C. L., Sakulyanontvittaya, T., Duhl, T., Emmons, L. K., and Wang, X.: The Model of

603   Emissions of Gases and Aerosols from Nature version 2.1 (MEGAN2.1): an extended and updated framework for modeling

604   biogenic emissions, Geosci. Model Dev., 5, 1471–1492, https://doi.org/10.5194/gmd-5-1471-2012, 2012.

605   Herman, J., Cede, A., Spinei, E., Mount, G., Tzortziou, M., and Abuhassan, N.: NO_2 column amounts from ground-based

606   Pandora and MFDOAS spectrometers using the direct-sun DOAS technique: Intercomparisons and application to OMI

607   validation, J. Geophys. Res., 114, D13307, https://doi.org/10.1029/2009JD011848, 2009.

608   Herman, J., Spinei, E., Fried, A., Kim, J., Kim, J., Kim, W., Cede, A., Abuhassan, N., and Segal-Rozenhaimer, M.: NO_2 and

609   HCHO measurements in Korea from 2012 to 2016 from Pandora spectrometer instruments compared with OMI retrievals and

610   with aircraft measurements during the KORUS-AQ campaign, Atmos. Meas. Tech., 11, 4583–4603,

611   https://doi.org/10.5194/amt-11-4583-2018, 2018.

612   Hong, H., Lee, H., Kim, J., Jeong, U., Ryu, J., and Lee, D.: Investigation of Simultaneous Effects of Aerosol Properties and

613   Aerosol Peak Height on the Air Mass Factors for Space-Borne NO_2 Retrievals, Remote Sensing, 9, 208,

614   https://doi.org/10.3390/rs9030208, 2017.

615   Jeong, U., and H. Hong: Assessment of tropospheric concentrations of NO_2 from the TROPOMI/Sentinel-5 Precursor for the

616   estimation of long-term exposure to surface NO_2 over South Korea, Remote Sensing, 13, 1877,

617   https://doi.org/10.3390/rs13101877, 2021a.

618   Jeong, U., and H. Hong: Comparison of total column and surface mixing ratio of carbon monoxide derived from the

619   TROPOMI/Sentinel-5 Precursor with In-Situ measurements from extensive ground-based network over South Korea, Remote

620   Sensing, 13, 3987, https://doi.org/10.3390/rs13193987, 2021b.

621   Judd, L. M., Al-Saadi, J. A., Valin, L. C., Pierce, R. B., Yang, K., Janz, S. J., Kowalewski, M. G., Szykman, J. J., Tiefengraber,

622   M., and Mueller, M.: The Dawn of Geostationary Air Quality Monitoring: Case Studies From Seoul and Los Angeles, Front.

623   Environ. Sci., 6, 85, https://doi.org/10.3389/fenvs.2018.00085, 2018.

624   Judd, L. M., Al-Saadi, J. A., Janz, S. J., Kowalewski, M. G., Pierce, R. B., Szykman, J. J., Valin, L. C., Swap, R., Cede, A.,

625   Mueller, M., Tiefengraber, M., Abuhassan, N., and Williams, D.: Evaluating the impact of spatial resolution on tropospheric

626   NO_2 column comparisons within urban areas using high-resolution airborne data, Atmos. Meas. Tech., 12, 6091–6111,

627   https://doi.org/10.5194/amt-12-6091-2019, 2019.

628   Judd, L. M., Al-Saadi, J. A., Szykman, J. J., Valin, L. C., Janz, S. J., Kowalewski, M. G., Eskes, H. J., Veefkind, J. P., Cede,

629   A., Mueller, M., Gebetsberger, M., Swap, R., Pierce, R. B., Nowlan, C. R., Abad, G. G., Nehrir, A., and Williams, D.:

630   Evaluating Sentinel-5P TROPOMI tropospheric NO_2 column densities with airborne and Pandora spectrometers near New

631   York City and Long Island Sound, Atmos. Meas. Tech., 13, 6113–6140, https://doi.org/10.5194/amt-13-6113-2020, 2020.

632   Kendrick, C. M., Koonce, P., and George, L. A.: Diurnal and seasonal variations of NO, NO_2 and $PM_{2.5}$ mass as a function of

633   traffic volumes alongside an urban arterial, Atmospheric Environment, 122, 133–141,

634   https://doi.org/10.1016/j.atmosenv.2015.09.019, 2015.

635 Kim, D., Lee, H., Hong, H., Choi, W., Lee, Y., and Park, J.: Estimation of Surface NO_2 Volume Mixing Ratio in Four
636 Metropolitan Cities in Korea Using Multiple Regression Models with OMI and AIRS Data, Remote Sensing, 9, 627,
637 https://doi.org/10.3390/rs9060627, 2017.

638 Kim, J., Jeong, U., Ahn, M.-H., Kim, J. H., Park, R. J., Lee, H., Song, C. H., Choi, Y.-S., Lee, K.-H., Yoo, J.-M., Jeong, M.-
639 J., Park, S. K., Lee, K.-M., Song, C.-K., Kim, S.-W., Kim, Y. J., Kim, S.-W., Kim, M., Go, S., Liu, X., Chance, K., Chan
640 Miller, C., Al-Saadi, J., Veihelmann, B., Bhartia, P. K., Torres, O., Abad, G. G., Haffner, D. P., Ko, D. H., Lee, S. H., Woo,
641 J.-H., Chong, H., Park, S. S., Nicks, D., Choi, W. J., Moon, K.-J., Cho, A., Yoon, J., Kim, S., Hong, H., Lee, K., Lee, H., Lee,
642 S., Choi, M., Veefkind, P., Levelt, P. F., Edwards, D. P., Kang, M., Eo, M., Bak, J., Baek, K., Kwon, H.-A., Yang, J., Park, J.,
643 Han, K. M., Kim, B.-R., Shin, H.-W., Choi, H., Lee, E., Chong, J., Cha, Y., Koo, J.-H., Irie, H., Hayashida, S., Kasai, Y.,
644 Kanaya, Y., Liu, C., Lin, J., Crawford, J. H., Carmichael, G. R., Newchurch, M. J., Lefer, B. L., Herman, J. R., Swap, R. J.,
645 Lau, A. K. H., Kurosu, T. P., Jaross, G., Ahlers, B., Dobber, M., McElroy, C. T., and Choi, Y.: New Era of Air Quality
646 Monitoring from Space: Geostationary Environment Monitoring Spectrometer (GEMS), 101, E1–E22,
647 https://doi.org/10.1175/BAMS-D-18-0013.1, 2020.

648 Kley, D. and McFarland, M.: Chemiluminescence detector for NO and NO_2, Atmos. Technol.; (United States), 12, 1980.

649 Kowalewski, M. G. and Janz, S. J.: Remote sensing capabilities of the GEO-CAPE airborne simulator, SPIE Optical
650 Engineering + Applications, San Diego, California, United States, 92181I, https://doi.org/10.1117/12.2062058, 2014.

651 Kowalewski, M.G., Janz, S., Al-Saadi, J.A., Good, W., Ruppert, L., Cole, J.: GeoTASO instrument characterization and
652 level1b radiance product generation, In: Proceedings of the 1st KORUS-AQ Science Team Meeting, Jeju, South Korea, 27
653 February–3 March 2017, 13. 2017

654 Lamsal, L. N., Martin, R. V., Parrish, D. D., and Krotkov, N. A.: Scaling Relationship for NO_2 Pollution and Urban Population
655 Size: A Satellite Perspective, Environ. Sci. Technol., 47, 7855–7861, https://doi.org/10.1021/es400744g, 2013.

656 Lamsal, L. N., Janz, S. J., Krotkov, N. A., Pickering, K. E., Spurr, R. J. D., Kowalewski, M. G., Loughner, C. P., Crawford, J.
657 H., Swartz, W. H., and Herman, J. R.: High-resolution NO_2 observations from the Airborne Compact Atmospheric Mapper:
658 Retrieval and validation, J. Geophys. Res. Atmos., 122, 1953–1970, https://doi.org/10.1002/2016JD025483, 2017.

659 Latza, U., Gerdes, S., and Baur, X.: Effects of nitrogen dioxide on human health: Systematic review of experimental and
660 epidemiological studies conducted between 2002 and 2006, International Journal of Hygiene and Environmental Health, 212,
661 271–287, https://doi.org/10.1016/j.ijheh.2008.06.003, 2009.

662 Lee, K., Yu, J., Lee, S., Park, M., Hong, H., Park, S. Y., Choi, M., Kim, J., Kim, Y., Woo, J.-H., Kim, S.-W., and Song, C. H.:
663 Development of Korean Air Quality Prediction System version 1 (KAQPS v1) with focuses on practical issues, Geosci. Model
664 Dev., 13, 1055–1073, https://doi.org/10.5194/gmd-13-1055-2020, 2020.

665 Leitão, J., Richter, A., Vrekoussis, M., Kokhanovsky, A., Zhang, Q. J., Beekmann, M., and Burrows, J. P.: On the improvement
666 of NO_2 satellite retrievals–aerosol impact on the airmass factors, Atmos. Meas. Tech., 3, 475–493, https://doi.org/10.5194/amt-
667 3-475-2010, 2010.

668 Leitch, J. W., Delker, T., Good, W., Ruppert, L., Murcray, F., Chance, K., Liu, X., Nowlan, C., Janz, S. J., Krotkov, N. A.,

669 Pickering, K. E., Kowalewski, M., and Wang, J.: The GeoTASO airborne spectrometer project, SPIE Optical Engineering +

670 Applications, San Diego, California, United States, 92181H, https://doi.org/10.1117/12.2063763, 2014.

671 Levelt, P. F., van den Oord, G. H. J., Dobber, M. R., Malkki, A., Huib Visser, Johan de Vries, Stammes, P., Lundell, J. O. V.,

672 and Saari, H.: The ozone monitoring instrument, IEEE Trans. Geosci. Remote Sensing, 44, 1093–1101,

673 https://doi.org/10.1109/TGRS.2006.872333, 2006.

674 Lorente, A., Folkert Boersma, K., Yu, H., Dörner, S., Hilboll, A., Richter, A., Liu, M., Lamsal, L. N., Barkley, M., De Smedt,

675 I., Van Roozendael, M., Wang, Y., Wagner, T., Beirle, S., Lin, J.-T., Krotkov, N., Stammes, P., Wang, P., Eskes, H. J., and

676 Krol, M.: Structural uncertainty in air mass factor calculation for NO_2 and HCHO satellite retrievals, Atmos. Meas. Tech., 10,

677 759–782, https://doi.org/10.5194/amt-10-759-2017, 2017.

678 Ma, J. Z., Beirle, S., Jin, J. L., Shaiganfar, R., Yan, P., and Wagner, T.: Tropospheric NO_2 vertical column densities over

679 Beijing: results of the first three years of ground-based MAX-DOAS measurements (2008–2011) and satellite validation,

680 Atmos. Chem. Phys., 13, 1547–1567, https://doi.org/10.5194/acp-13-1547-2013, 2013.

681 Malm, W. C. and Hand J. L.: An examination of the physical and optical properties of aerosols collected in the IMPROVE

682 program, Atmospheric Environment, 41, 3407– 3427, https://doi.org/10.1016/j.atmosenv.2006.12.012, 2007.

683 Merlaud, A., Constantin, D., Mingireanu, F., Mocanu, I., Maes, J., Fayt, C., Voiculescu, M., Murariu, G., Georgescu, L., Van

684 Roozendael, M.: Small whiskbroom imager for atmospheric composition monitoring (SWING) from an unmanned aerial

685 vehicle (UAV), in: Proceedings of the 21st ESA Symposium on European Rocket & Balloon Programmes and related Research,

686 Thun, Switzerland pp.9–13, 2013.

687 Meier, A. C., Schönhardt, A., Bösch, T., Richter, A., Seyler, A., Ruhtz, T., Constantin, D.-E., Shaiganfar, R., Wagner, T.,

688 Merlaud, A., Van Roozendael, M., Belegante, L., Nicolae, D., Georgescu, L., and Burrows, J. P.: High-resolution airborne

689 imaging DOAS measurements of NO_2 above Bucharest during AROMAT, Atmos. Meas. Tech., 10, 1831–1857,

690 https://doi.org/10.5194/amt-10-1831-2017, 2017.

691 Merlaud, A., Tack, F., Constantin, D., Georgescu, L., Maes, J., Fayt, C., Mingireanu, F., Schuettemeyer, D., Meier, A. C.,

692 Schönardt, A., Ruhtz, T., Bellegante, L., Nicolae, D., Den Hoed, M., Allaart, M., and Van Roozendael, M.: The Small

693 Whiskbroom Imager for atmospheric compositioN monitorinG (SWING) and its operations from an unmanned aerial vehicle

694 (UAV) during the AROMAT campaign, Atmos. Meas. Tech., 11, 551–567, https://doi.org/10.5194/amt-11-551-2018, 2018.

695 Nowlan, C. R., Liu, X., Leitch, J. W., Chance, K., González Abad, G., Liu, C., Zoogman, P., Cole, J., Delker, T., Good, W.,

696 Murcray, F., Ruppert, L., Soo, D., Follette-Cook, M. B., Janz, S. J., Kowalewski, M. G., Loughner, C. P., Pickering, K. E.,

697 Herman, J. R., Beaver, M. R., Long, R. W., Szykman, J. J., Judd, L. M., Kelley, P., Luke, W. T., Ren, X., and Al-Saadi, J. A.:

698 Nitrogen dioxide observations from the Geostationary Trace gas and Aerosol Sensor Optimization (GeoTASO) airborne

699 instrument: Retrieval algorithm and measurements during DISCOVER-AQ Texas 2013, Atmos. Meas. Tech., 9, 2647–2668,

700 https://doi.org/10.5194/amt-9-2647-2016, 2016.

701 National Institute of Environmental Research (NIER) and National Aeronautics and Space Administration (NASA): KORUS-

702 AQ Final Science Synthesis Report, available at https://espo.nasa.gov/sites/default/files/documents/5858211.pdf, last access:

703 27 June 2022, 2020.

704 Nowlan, C. R., Liu, X., Leitch, J. W., Chance, K., A., González Abad, Liu, C., Zoogman, P., Cole, J., Delker, T., Good, W.,

705 Murcray, F., Ruppert, L., Soo, D., Follette-Cook, M. B., Janz, S. J., Kowalewski, M. G., Loughner, C. P., Pickering,K. E.,

706 Herman, J. R., Beaver, M. R., Long, R. W., Szykman, J. J., Judd, L. M., Kelley, P., Luke, W. T., Ren, W., and Sl-Saadi, J. A.:

707 Nitrogen dioxide observations from the Geostationary Trace gas and Aerosol Sensor Optimization (GeoTASO) airborne

708 instrument: Retrieval algorithm and measurements during DISCOVER-AQ Texas 2013, Atmos. Meas. Tech., 9, 2647-2668,

709 http://doi.org/10.5194/atm-9-2647-2016, 2016.

710 Nowlan, C. R., Liu, X., Janz, S. J., Kowalewski, M. G., Chance, K., Follette-Cook, M. B., Fried, A., González Abad, G.,

711 Herman, J. R., Judd, L. M., Kwon, H.-A., Loughner, C. P., Pickering, K. E., Richter, D., Spinei, E., Walega, J., Weibring, P.,

712 and Weinheimer, A. J.: Nitrogen dioxide and formaldehyde measurements from the GEOstationary Coastal and Air Pollution

713 Events (GEO-CAPE) Airborne Simulator over Houston, Texas, Atmos. Meas. Tech., 11, 5941–5964,

714 https://doi.org/10.5194/amt-11-5941-2018, 2018.

715 Palmer, P. I., Jacob, D. J., Chance, K., Martin, R. V., Spurr, R. J. D., Kurosu, T. P., Bey, I., Yantosca, R., Fiore, A., and Li,

716 Q.: Air mass factor formulation for spectroscopic measurements from satellites: Application to formaldehyde retrievals from

717 the Global Ozone Monitoring Experiment, J. Geophys. Res., 106, 14539–14550, https://doi.org/10.1029/2000JD900772, 2001.

718 Pastel, M., Pommereau, J.-P., Goutail, F., Richter, A., Pazmiño, A., Ionov, D., and Portafaix, T.: Construction of merged

719 satellite total O_3 and NO_2 time series in the tropics for trend studies and evaluation by comparison to NDACC SAOZ

720 measurements, Atmos. Meas. Tech., 7, 3337–3354, https://doi.org/10.5194/amt-7-3337-2014, 2014.

721 Platt, U.: Differential absorption spectroscopy (DOAS), Chem. Anal. Series, 127, 27–83, 1994.

722 Platt, U., Stutz, J.: Differential absorption spectroscopy, in: Differential Optical Absorption Spectroscopy, Springer, Berlin,

723 Heidelberg, pp. 135–174, 2008.

724 Popp, C., Brunner, D., Damm, A., Van Roozendael, M., Fayt, C., and Buchmann, B.: High-resolution NO_2 remote sensing

725 from the Airborne Prism EXperiment (APEX) imaging spectrometer, Atmos. Meas. Tech., 5, 2211–2225,

726 https://doi.org/10.5194/amt-5-2211-2012, 2012.

727 Prasad, A. K., Singh, R. P., and Kafatos, M.: Influence of coal-based thermal power plants on the spatial–temporal variability

728 of tropospheric NO_2 column over India, Environ Monit Assess, 184, 1891–1907, https://doi.org/10.1007/s10661-011-2087-6,

729 2012.

730 Qin, K., Rao, L., Xu, J., Bai, Y., Zou, J., Hao, N., Li, S., and Yu, C.: Estimating Ground Level NO_2 Concentrations over

731 Central-Eastern China Using a Satellite-Based Geographically and Temporally Weighted Regression Model, Remote Sensing,

732 9, 950, https://doi.org/10.3390/rs9090950, 2017.

733 Richter, A., Burrows, J. P., Nüß, H., Granier, C., and Niemeier, U.: Increase in tropospheric nitrogen dioxide over China

734 observed from space, Nature, 437, 129–132, https://doi.org/10.1038/nature04092, 2005.

735 Schönhardt, A., Altube, P., Gerilowski, K., Krautwurst, S., Hartmann, J., Meier, A. C., Richter, A., and Burrows, J. P.: A wide

736 field-of-view imaging DOAS instrument for two-dimensional trace gas mapping from aircraft, Atmos. Meas. Tech., 8, 5113–

737 5131, https://doi.org/10.5194/amt-8-5113-2015, 2015.

738 Shah, V., Jacob, D. J., Li, K., Silvern, R. F., Zhai, S., Liu, M., Lin, J., and Zhang, Q.: Effect of changing NOx lifetime on the

739 seasonality and long-term trends of satellite-observed tropospheric NO_2 columns over China, Atmos. Chem. Phys., 20, 1483–

740 1495, https://doi.org/10.5194/acp-20-1483-2020, 2020.

741 Skamarock, W., Klemp, J., Dudhia, J., Gill, D., Barker, D., Wang, W., Huang, X.-Y., and Duda, M.: A Description of the

742 Advanced Research WRF Version 3, UCAR/NCAR, https://doi.org/10.5065/D68S4MVH, 2008.

743 Spinei, E., Whitehill, A., Fried, A., Tiefengraber, M., Knepp, T. N., Herndon, S., Herman, J. R., Müller, M., Abuhassan, N.,

744 Cede, A., Richter, D., Walega, J., Crawford, J., Szykman, J., Valin, L., Williams, D. J., Long, R., Swap, R. J., Lee, Y., Nowak,

745 N., and Poche, B.: The first evaluation of formaldehyde column observations by improved Pandora spectrometers during the

746 KORUS-AQ field study, Atmos. Meas. Tech., 11, 4943–4961, https://doi.org/10.5194/amt-11-4943-2018, 2018.

747 Spurr, R. and Christi, M.: On the generation of atmospheric property Jacobians from the (V)LIDORT linearized radiative

748 transfer models, Journal of Quantitative Spectroscopy and Radiative Transfer, 142, 109–115,

749 https://doi.org/10.1016/j.jqsrt.2014.03.011, 2014.

750 Tack, F., Merlaud, A., Iordache, M.-D., Danckaert, T., Yu, H., Fayt, C., Meuleman, K., Deutsch, F., Fierens, F., and Van

751 Roozendael, M.: High-resolution mapping of the NO_2 spatial distribution over Belgian urban areas based on airborne APEX

752 remote sensing, Atmos. Meas. Tech., 10, 1665–1688, https://doi.org/10.5194/amt-10-1665-2017, 2017.

753 Tack, F., Merlaud, A., Meier, A. C., Vlemmix, T., Ruhtz, T., Iordache, M.-D., Ge, X., van der Wal, L., Schuettemeyer, D.,

754 Ardelean, M., Calcan, A., Constantin, D., Schönhardt, A., Meuleman, K., Richter, A., and Van Roozendael, M.:

755 Intercomparison of four airborne imaging DOAS systems for tropospheric NO_2 mapping–the AROMAPEX campaign, Atmos.

756 Meas. Tech., 12, 211–236, https://doi.org/10.5194/amt-12-211-2019, 2019.

757 Tack, F., Merlaud, A., Iordache, M.-D., Pinardi, G., Dimitropoulou, E., Eskes, H., Bomans, B., Veefkind, P., and Van

758 Roozendael, M.: Assessment of the TROPOMI tropospheric NO_2 product based on airborne APEX observations, Atmos. Meas.

759 Tech., 14, 615–646, https://doi.org/10.5194/amt-14-615-2021, 2021.

760 Tzortziou, M., Parker, O., Lamb, B., Herman, J., Lamsal, L., Stauffer, R., and Abuhassan, N.: Atmospheric Trace Gas (NO_2

761 and O_3) Variability in South Korean Coastal Waters, and Implications for Remote Sensing of Coastal Ocean Color Dynamics,

762 Remote Sensing, 10, 1587, https://doi.org/10.3390/rs10101587, 2018.

763 Valks, P., Pinardi, G., Richter, A., Lambert, J.-C., Hao, N., Loyola, D., Van Roozendael, M., and Emmadi, S.: Operational

764 total and tropospheric NO_2 column retrieval for GOME-2, Atmos. Meas. Tech., 4, 1491–1514, https://doi.org/10.5194/amt-4-

765 1491-2011, 2011.

766 Vandaele, A. C., Hermans, C., Simon, P. C., Carleer, M., Colin, R., Fally, S., Mérienne, M. F., Jenouvrier, A., and Coquart,

767 B.: Measurements of the NO_2 absorption cross-section from $42\,000\ \text{cm}^{-1}$ to $10\,000\ \text{cm}^{-1}$ (238−1000 nm) at 220 K and 294 K,

Journal of Quantitative Spectroscopy and Radiative Transfer, 59, 171–184, https://doi.org/10.1016/S0022-4073(97)00168-4, 1998.

Veefkind, J. P., Aben, I., McMullan, K., Förster, H., de Vries, J., Otter, G., Claas, J., Eskes, H. J., de Haan, J. F., Kleipool, Q., van Weele, M., Hasekamp, O., Hoogeveen, R., Landgraf, J., Snel, R., Tol, P., Ingmann, P., Voors, R., Kruizinga, B., Vink, R., Visser, H., and Levelt, P. F.: TROPOMI on the ESA Sentinel-5 Precursor: A GMES mission for global observations of the atmospheric composition for climate, air quality and ozone layer applications, Remote Sensing of Environment, 120, 70–83, https://doi.org/10.1016/j.rse.2011.09.027, 2012.

Vlemmix, T., Ge, X., de Goeij, B. T. G., van der Wal, L. F., Otter, G. C. J., Stammes, P., Wang, P., Merlaud, A., Schüttemeyer, D., Meier, A. C., Veefkind, J. P., and Levelt, P. F.: Retrieval of tropospheric NO_2 columns over Berlin from high-resolution airborne observations with the spectrolite breadboard instrument, Atmos. Meas. Tech. Discuss., https://doi.org/10.5194/amt-2017-257, in review, 2017.

Wiedinmyer, C., Quayle, B., Geron, C., Belote, A., McKenzie, D., Zhang, X., O'Neill, S., and Wynne, K. K.: Estimating emissions from fires in North America for air quality modeling, Atmospheric Environment, 40, 3419–3432, https://doi.org/10.1016/j.atmosenv.2006.02.010, 2006.

Wiedinmyer, C., Akagi, S. K., Yokelson, R. J., Emmons, L. K., Al-Saadi, J. A., Orlando, J. J., and Soja, A. J.: The Fire INventory from NCAR (FINN): a high resolution global model to estimate the emissions from open burning, Geosci. Model Dev., 4, 625–641, https://doi.org/10.5194/gmd-4-625-2011, 2011.

Wold, S., Esbensen, K., and Geladi, P.: Principal component analysis, Chemometrics and Intelligent Laboratory Systems, 2, 37–52, https://doi.org/10.1016/0169-7439(87)80084-9, 1987.

Woo, J.-H., Choi, K.-C., Kim, H. K., Baek, B. H., Jang, M., Eum, J.-H., Song, C. H., Ma, Y.-I., Sunwoo, Y., Chang, L.-S., and Yoo, S. H.: Development of an anthropogenic emissions processing system for Asia using SMOKE, Atmospheric Environment, 58, 5–13, https://doi.org/10.1016/j.atmosenv.2011.10.042, 2012.

Zoogman, P., Liu, X., Suleiman, R. M., Pennington, W. F., Flittner, D. E., Al-Saadi, J. A., Hilton, B. B., Nicks, D. K., Newchurch, M. J., Carr, J. L., Janz, S. J., Andraschko, M. R., Arola, A., Baker, B. D., Canova, B. P., Chan Miller, C., Cohen, R. C., Davis, J. E., Dussault, M. E., Edwards, D. P., Fishman, J., Ghulam, A., González Abad, G., Grutter, M., Herman, J. R., Houck, J., Jacob, D. J., Joiner, J., Kerridge, B. J., Kim, J., Krotkov, N. A., Lamsal, L., Li, C., Lindfors, A., Martin, R. V., McElroy, C. T., McLinden, C., Natraj, V., Neil, D. O., Nowlan, C. R., O'Sullivan, E. J., Palmer, P. I., Pierce, R. B., Pippin, M. R., Saiz-Lopez, A., Spurr, R. J. D., Szykman, J. J., Torres, O., Veefkind, J. P., Veihelmann, B., Wang, H., Wang, J., and Chance, K.: Tropospheric emissions: Monitoring of pollution (TEMPO), Journal of Quantitative Spectroscopy and Radiative Transfer, 186, 17–39, https://doi.org/10.1016/j.jqsrt.2016.05.008, 2017.